DISCRETE AND CONTINUOUS
DYNAMICAL SYSTEMS
Volume **29**, Number **4**, April **2011**

doi:10.3934/dcds.2011.29.xx

pp. **1–XX**

INVESTIGATING THE CONSEQUENCES OF GLOBAL BIFURCATIONS FOR TWO-DIMENSIONAL INVARIANT MANIFOLDS OF VECTOR FIELDS

Pablo Aguirre[a], Eusebius J. Doedel[b], Bernd Krauskopf[a] and Hinke M. Osinga[a]

[a] Bristol Centre for Applied Nonlinear Mathematics
Department of Engineering Mathematics
University of Bristol
Bristol BS8 1TR, United Kingdom

[b] Department of Computer Science
Concordia University
1455 Boulevard de Maisonneuve O.
Montréal, Québec H3G 1M8, Canada

Abstract. We consider a homoclinic bifurcation of a vector field in $\mathbb{R}^3$, where a one-dimensional unstable manifold of an equilibrium is contained in the two-dimensional stable manifold of this same equilibrium. How such one-dimensional connecting orbits arise is well understood, and software packages exist to detect and follow them in parameters.

In this paper we address an issue that it is far less well understood: how does the associated two-dimensional stable manifold change geometrically during the given homoclinic bifurcation? This question can be answered with the help of advanced numerical techniques. More specifically, we compute two-dimensional manifolds, and their one-dimensional intersection curves with a suitable cross-section, via the numerical continuation of orbit segments as solutions of a boundary value problem. In this way, we are able to explain how homoclinic bifurcations may lead to quite dramatic changes of the overall dynamics. This is demonstrated with two examples. We first consider a Shilnikov bifurcation in a semiconductor laser model, and show how the associated change of the two-dimensional stable manifold results in the creation of a new basin of attraction. We then investigate how the basins of the two symmetrically related attracting equilibria change to give rise to preturbulence in the first homoclinic explosion of the Lorenz system.

1. **Introduction.** Numerous areas of application give rise to mathematical models that can be written in the form of an autonomous vector field; see, for example, the textbooks [25, 41, 62] and further references therein. The main task is then to determine the possible dynamics of the system, which means that one needs to find the compact invariant objects (such as equilibria and periodic orbits) and, when they are of saddle type, their stable and unstable invariant manifolds. Furthermore, the question arises how these objects change with system parameters. Changes of the local stability of equilibria and periodic orbits give rise to local bifurcations that can be understood via normal forms. However, one also needs to consider how the global

2000 *Mathematics Subject Classification.* Primary: 34C45, 34C37; Secondary: 65L10.
Key words and phrases. Homoclinic bifurcation, invariant manifolds, boundary value problem.

dynamics changes due to re-arrangements of stable and unstable manifolds. At such a global bifurcation one finds homoclinic and heteroclinic connecting orbits from a saddle object back to itself or to a second saddle object, respectively. It is well known that homoclinic and heteroclinic bifurcations are important for understanding the overall dynamics. In particular, they play a key role in transitions from simple to complicated dynamics; see, for example, the textbooks [25, 41, 59] and the recent survey paper [30] as entry points to the extensive literature.

In this paper we consider the consequences of a global bifurcation for the overall organization of the dynamics by the stable and unstable manifolds — both near the connecting orbit and further away from it. More specifically, we focus on homoclinic bifurcations of equilibria in three-dimensional vector fields as the simplest class of examples where this question is of interest. Throughout, we consider a vector field

$$\dot{x} = f(x, \lambda), \tag{1}$$

where $x \in \mathbb{R}^3$, $\lambda \in \mathbb{R}^m$ is a parameter vector, and $f : \mathbb{R}^3 \times \mathbb{R}^m \to \mathbb{R}^3$ is sufficiently smooth. The vector field (1) induces a flow φ^t on $\mathbb{R}^3$ that determines the dynamics. We suppose that (1) has a hyperbolic saddle equilibrium p, meaning that the Jacobian matrix $Df(p)$ has only eigenvalues with both positive or negative real parts (and none with zero real part), which come with associated stable and unstable eigenspaces $E^s(p)$ and $E^u(p)$. The global stable and unstable manifolds of p are then defined as

$$W^s(p) = \left\{x \in \mathbb{R}^3 \mid \varphi^t(x) \to p \text{ as } t \to \infty\right\}$$

and

$$W^u(p) = \left\{x \in \mathbb{R}^3 \mid \varphi^t(x) \to p \text{ as } t \to -\infty\right\} .$$

According to the Stable Manifold Theorem [50], $W^s(p)$ and $W^u(p)$ are (immersed) manifolds that are as smooth as f and tangent at p to $E^s(p)$ and $E^u(p)$, respectively. Without loss of generality, we assume that $E^u(p)$ and $W^u(p)$ are of dimension one, and $E^s(p)$ and $W^s(p)$ are of dimension two. (Note that this can always be achieved by reversing time if necessary.)

We consider a homoclinic orbit of (1) that connects the equilibrium p back to itself. In our setting the homoclinic orbit is formed by one branch of the one-dimensional unstable manifold $W^u(p)$, which lies entirely in the surface $W^s(p)$. Provided that certain transversality conditions are satisfied, the situation is of codimension one, meaning that it occurs at an isolated value λ^* when a single parameter $\lambda \in \mathbb{R}$ is changed. In the simplest case, a single periodic orbit bifurcates but more complicated and even chaotic dynamics may be found as well; see, for example, [30, 59].

It is an interesting observation that homoclinic bifurcations (and global bifurcations more generally) are studied and illustrated in the literature with an emphasis on the *one-dimensional* unstable manifold that forms the connecting orbit. The associated stable manifold of higher dimension is generally considered only *locally near the connecting orbit*, for example, in intersection with a local section. Such illustrations are mostly in the form of topological sketches and they emphasise the theoretical point of view that it is sufficient to study global bifurcations in a tubular neighborhood of the one-dimensional connecting orbits.

By contrast, the emphasis of this paper is on how the *two-dimensional stable manifold changes* as the one-dimensional manifold 'passes through it' to form the homoclinic connection when a parameter is changed through the value where the

homoclinic bifurcation takes place. This allows us to investigate how the homoclinic bifurcation manifests itself throughout the entire phase space, and not just in a neighborhood of the homoclinic orbit. Of special interest in this context is how the basins of different attracting sets change in the global bifurcation under consideration. This question is not only of theoretical interest, but also relevant for the study of specific vector-field models arising in applications. In an application context a global bifurcation generally does not occur 'in isolation' but in the presence of other invariant objects. Hence, quantitative information about where basin boundaries are located is generally what is required. Since two-dimensional stable manifolds form boundaries of basins of attraction, their computation is the key to understanding how a given global bifurcation changes the overall dynamics, even very far away from where the homoclinic orbit appears in phase space.

A homoclinic orbit and the associated stable and unstable manifolds are global objects that normally do not have analytic expressions so that they need to be found numerically. Today, continuation software packages, such as AUTO [12], CONTENT [40] and MATCONT [10], are able, as a standard feature, to find a homoclinic orbit and then continue it in (at least two) parameters. One approach is to find a periodic orbit with sufficiently large period T, which can then be continued in two parameters as an approximation of the homoclinic orbit. A more reliable numerical method is to represent the homoclinic orbit itself as an orbit segment that starts near the equilibrium along the unstable eigenspace $E^u(p)$ and ends back near the equilibrium in the stable eigenspace $E^s(p)$. (One also speaks of projection boundary conditions, and error bounds can be derived for such an approximation as a function of the total integration time T of the orbit segment [5].) This method is implemented, for example, in the HOMCONT [8] extension of AUTO; see also [14, 21, 46]. HOMCONT also contains several test functions that allow one to detect and then continue (in at least three parameters) global bifurcations of these orbits up to codimension two. Furthermore, methods based on Lin's method [43] allow one to find even more complicated homoclinic and heteroclinic orbits with several close returns to a neighborhood of an equilibrium or periodic orbit [39, 46]. With these numerical tools it is possible to obtain very intricate bifurcation diagrams that feature global bifurcations of higher codimension as organising centers; see, for example, the recent studies [7, 65].

The computation of the associated stable and unstable manifolds, on the other hand, is much less standard today. While one-dimensional stable and unstable manifolds of vector fields are curves that can be found readily by integration, the computation of global invariant manifolds of dimension two (or higher) remains quite challenging. The development of computational tools for their computation has been an area of active research in recent years; see, for example, the recent surveys [35, 37]. The two-dimensional stable manifolds presented here have been computed via the continuation of orbit segments that are defined as solutions of suitable boundary value problems. More specifically, we employ and combine two methods that are based on complementary representations of a relevant part of the two-dimensional global manifold. One method computes the manifold as a family of orbit segments, and the other as a family of geodesic level sets; see Sec. 2 for more details. By visualizing the computed two-dimensional manifolds appropriately as surfaces in three-dimensional space, we obtain insight into the geometric consequences of the global bifurcation in question.

We bring these numerical methods to bear in the study of two concrete test-case examples. First, we consider a Shilnikov bifurcation (homoclinic orbit to a saddle-focus) in a model of a laser with optical injection [65, 66, 68]. We focus here on the case of a so-called simple Shilnikov bifurcation, where the saddle quantity at the equilibrium is negative so that a single attracting periodic orbit bifurcates [41]. Near this global bifurcation the laser system shows excitability: there is an attracting equilibrium nearby, and any perturbation past the two-dimensional stable manifold of the saddle focus leads to a large excursion corresponding to a pulse of laser light. We show in Sec. 3 how the two-dimensional stable manifold changes at the Shilnikov bifurcation to organize the overall dynamics. Our second example is the first homoclinic bifurcation (or explosion point) in the Lorenz system [15, 60]. Due to the symmetry of the Lorenz equations, there is a symmetric pair of homoclinic orbits in a butterfly configuration. The complex dynamics of the Lorenz system is created in this so-called homoclinic explosion in a tubular neighborhood of both homoclinic orbits. However, it is initially of a transitory nature (one speaks of preturbulence) after this bifurcation: before and after the bifurcation all typical orbits end up at one of two (symmetrically related) attracting equilibria. We show in Sec. 4 what the consequences of the homoclinic explosion are for the two-dimensional stable manifold of the origin, and how the two basins of attraction change dramatically in this transition to preturbulence.

Apart from being of immediate interest for the systems at hand, the case studies presented here also serve the purpose of highlighting what can be achieved with manifold computations. It is now possible to gain detailed global understanding of how the dynamics is organized by homoclinic and heteroclinic bifurcations in a three-dimensional vector field. We would also argue that the images in this paper represent the state-of-the-art in terms of computation and visualization of global invariant manifolds of vector fields. Clearly, there are many more global bifurcations that can be studied similarly, and Sec. 5 discusses directions of ongoing and future research.

2. Computing manifolds via the continuation of orbit segments.

Solvers for two-point boundary value problems (BVPs) are a key feature of numerical continuation software such as AUTO [12], CONTENT [40] and MATCONT [10]. In combination with path following, it is possible to find and then follow the solution of a well-posed BVP in parameters. We make extensive use of this capability for the computation of invariant manifolds by defining BVPs that specify families of orbit segments of interest. The general set-up can be formulated for autonomous vector fields in any space dimension, but we restrict here to the case of a three-dimensional phase space for simplicity; see [13, 35, 37] for more information. More specifically, we consider a function

$$\mathbf{u} : [0,1] \mapsto \mathbb{R}^3 \tag{2}$$

that satisfies the differential equation

$$\mathbf{u}'(t) \quad = \quad T\, f(\mathbf{u}(t)). \tag{3}$$

Note that (3) is simply the time-rescaled version of (1), where the integration time over the orbit segment is always 1; hence, the actual integration time in (1) appears as the explicit parameter T in (3). The function $\mathbf{u}$ represents a unique orbit segment provided that suitable boundary conditions are specified at one or both end points $\mathbf{u}(0)$ and $\mathbf{u}(1)$.

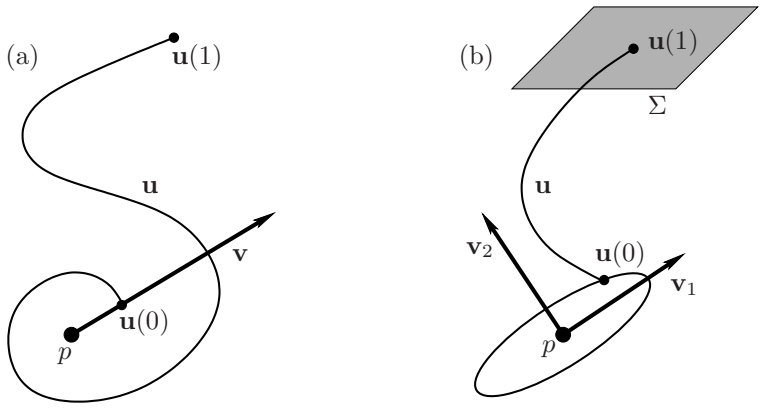

FIGURE 1. Sketch of an orbit segment $\mathbf{u}$ starting near an equilibrium p with complex eigenvalues (a) and with real eigenvalues (b). The second boundary condition can be left free or be constrained to lie in a two-dimensional submanifold Σ.

A convenient and powerful way of representing the orbit segment $\mathbf{u}$ numerically is the method known as collocation. It was first implemented in COLSYS [2], and first used in AUTO[11] in the context of bifurcation studies; later implementations include COLDAE [3], CONTENT [40], MATCONT [10], and other software packages. Here the function $\mathbf{u}$ is represented by polynomials of degree d in the intervals of a mesh with $N+1$ mesh points (where $\mathbf{u}(0)$ and $\mathbf{u}(1)$ are the first and last mesh points, respectively). One requires that the differential equation (3) is satisfied at certain interior points of the mesh intervals, namely, the so-called Gauss points. In conjunction with continuity constraints and the boundary conditions one obtains a set of equations that determines all $(d+1)\times N$ coefficients of the polynomials and the integration time T uniquely. We stress that a rigorous error analysis exists that shows the order (in terms of the maximal mesh size) at which the approximate solution converges to the true orbit segment; see [13] for details.

Once a numerical solution of the BVP has been found, it can readily be followed in a system parameter with standard pseudo-arclength continuation [13]. Indeed, this is the standard technique in AUTO, CONTENT and MATCONT for the continuation of a periodic orbit, which is represented as a solution of (3) subject to the boundary condition $\mathbf{u}(0)=\mathbf{u}(1)$ (plus a phase-condition), in which case the parameter is the period T. Similarly, a homoclinic orbit is represented in the HOMCONT extension of AUTO as a solution of (3) subject to the boundary conditions $\mathbf{u}(0)\in E^u(p)$ and $\mathbf{u}(1)\in E^s(p)$ (again, plus a phase-condition), where T needs to be sufficiently large to ensure the accuracy of the representation [5].

2.1. **Computing a 2D manifold as a family of orbit segments.** At the homoclinic bifurcation one knows a single orbit segment — the approximated homoclinic orbit — that lies in the two-dimensional manifold $W^s(p)$. We now explain how a large relevant part of $W^s(p)$ can be computed, regardless of whether this manifold is involved in a global bifurcation or not. The underlying idea is to represent a part of interest of $W^s(p)$ by a one-parameter family of orbit segments (of sufficient length), one end point of which lies in $E^s(p)$ and near p. More formally, the family is parameterized by a suitable one-dimensional submanifold in $E^s(p)$, where it is

convenient to distinguish between the cases that the stable eigenvalues λ_1^s and λ_2^s are complex or real.

When λ_1^s and λ_2^s are complex conjugate — as is the case for the Shilnikov bifurcation in Section 3 — we require that

$$\mathbf{u}(0) = p + \delta \mathbf{v}, \tag{4}$$

where $\mathbf{v} \in E^s(p)$ is a fixed vector of norm 1. Note that, throughout, we require that the point $\mathbf{u}(0)$ lies in $E^s(p)$, which means that the total integration time T in (3) of $\mathbf{u}$ is negative. As is illustrated in Fig. 1, the parameter δ parameterizes orbits that lie on $W^s(p)$ (to good approximation), provided that δ is sufficiently small to ensure that $E^s(p)$ is an accurate representation of $W^s(p)$ locally near p. Owing to the spiralling nature of the dynamics on $W^s(p)$ near p, it suffices to vary δ over a fixed small interval $[\delta_0, \delta_1)$; see Fig. 1. Note that the interval $[\delta_0, \delta_1)$ defines a fundamental domain on the vector $\mathbf{v}$, by which we mean that every orbit on (the approximation of) $W^s(p)$ intersects it exactly once. We remark that the boundary condition (4) can also be used to compute a stable (or unstable) manifold of a saddle periodic orbit. In this case the vector $\mathbf{v}$ is chosen from the stable (or unstable) linear bundle of the periodic orbit, which can also be found by continuation [39].

When λ_1^s and λ_2^s are real — as is the case for the Lorenz system in Section 4 — we can require, for example, that

$$\mathbf{u}(0) = p + \delta \left(\cos(\theta) \frac{\mathbf{v}_1}{|\lambda_1^s|} + \sin(\theta) \frac{\mathbf{v}_2}{|\lambda_2^s|} \right) \tag{5}$$

or variations thereof. The parameter $\theta \in [0, 2\pi)$ parameterizes orbits that lie on $W^s(p)$ (to good approximation) by an ellipse in $E^s(p)$, whose half-axes are determined by the ratio of the stable eigenvalues. Here, we again assume that δ is fixed at a sufficiently small value to ensure that $E^s(p)$ is an accurate representation of $W^s(p)$. Taking an ellipse, rather than a circle, of boundary conditions is helpful in the computations because it adjusts for the different rates of growth of orbits near p. We remark that it is preferable in practice to use boundary condition (4) over (5) when the eigenvalues are complex conjugate, because it is difficult to choose an ellipse in $E^s(p)$ to which the (spiralling) flow is transverse throughout; see, for example, [19]. Namely, for most ellipses one will find four points where the spiralling flow is tangent to the ellipse, which means that parts of the manifolds are covered twice as θ is continued over $[0, 2\pi)$. This issue is avoided entirely by boundary condition (4), because a spiralling flow is transverse to any vector $\mathbf{v} \in E^s(p)$.

Each of the boundary conditions (4) and (5) requires $\mathbf{u}(0)$ to lie on a one-dimensional curve, and this can be expressed by two equations for the three coordinate components of $\mathbf{u}(0)$. Hence, to obtain a representation of a part of $W^s(p)$ as a one-parameter family of orbit segments, we need to ensure that the defining family of BVPs is well-posed (i.e., has a unique solution for each value of δ and θ). This requires us to specify one additional condition [13].

2.1.1. *Continuation in the integration time.* For any fixed value $T = T_0$ of the total integration time, the BVP (3) with boundary conditions (4) for fixed δ, or alternatively (5) for fixed θ, has a unique solution. It is given by the initial value problem that is specified by $\mathbf{u}(0)$ after integration over time T_0, where T_0 is negative since we are considering a stable manifold. Hence, continuation in T, for example, with the package AUTO, does not change $\mathbf{u}(0)$, but the other end point $\mathbf{u}(1)$ traces out the unique orbit through $\mathbf{u}(0)$. In other words, starting from the trivial solution

$\mathbf{u}(0) = \mathbf{u}(1)$ for $T = 0$, this continuation amounts to solving the initial value problem with a collocation method. While this may seem like a complicated way of integrating from an specific initial condition, it has the benefit that the output files of this continuation method in AUTO are then compatible with subsequent steps of computing the manifold $W^s(p)$. Moreover, this approach is more likely to notice sensitive dependence on initial conditions and, therefore, it is less likely to compute the inaccurate or even spurious solutions that initial value solvers are prone to produce in such situations.

To obtain this first orbit on $W^s(p)$, one can monitor a user-defined function (a suitable end-point condition) during the continuation in T and detect an initial orbit that satisfies a further (boundary) condition. There are several choices, which makes this general approach rather flexible.

2.1.2. *Fixing integration time or arclength.* Arguably the simplest approach for defining a family of orbit segments on $W^s(p)$ is to stop the first continuation run at a suitable fixed integration time $T = T_0$ and subsequently continue solutions of (3) subject to (4) (or (5)) in the distance parameter δ (or the angle parameter θ). In this way, a first piece of $W^s(p)$ is swept out by orbit segments with the same integration time T_0, but with different arclengths.

Alternatively, the total arclength of the orbit segment of the family may be kept fixed, which means that a first piece of $W^s(p)$ is swept out by orbits of the same arclength, but with different integration times. To this end, one imposes the integral constraint

$$\int_0^1 T \ \| f(\mathbf{u}(s)) \| \ ds - L = 0 \tag{6}$$

along the orbit segment, while solving (3) subject to (4) (or (5)), where the integration time T and the distance δ (or the angle θ) are the continuation parameters. Here the arclength L is kept at a desired fixed value $L = L_0$; an initial orbit for this type of continuation can be obtained by monitoring L with a AUTO user-defined function during the continuation in T of Sec. 2.1.1.

It may be advantageous in certain calculations to fix the product $L \times T$, where L is the total arclength along the orbit segment as defined above. This approach has been used in [15] to compute orbit segments on the stable manifold of the Lorenz system past structurally stable heteroclinic connections. In this situation, $T \to \infty$ while the arclength L reaches a finite minimal value given by the length of the respective heteroclinic connection. By fixing $L \times T$, connecting orbits in the Lorenz system have been identified as minima of the arclength (or the norm of the solution) during the continuation in the distance parameter δ in (4); see [15] for details.

It is important to note that in all computations of $W^s(p)$ via parameterized families of orbit segments, each continuation step in AUTO is taken in the full product space of the (discretized) functions $\mathbf{u}(\cdot)$ and the parameters. That is, the continuation step size is not determined by a fixed variation of the initial condition, but by the change of the norm of the entire orbit segment. In this way, a good mesh resolution of the computed piece of $W^s(p)$ is achieved; see also [13].

2.1.3. *Intersection curves of $W^s(p)$ with a section.* To learn more about the structure of a two-dimensional stable manifold $W^s(p)$ it may be useful to compute intersection curves of $W^s(p)$ with a two-dimensional section given, say, as the zero set Σ of a vector function $G : \mathbb{R}^3 \to \mathbb{R}$. Note that $W^s(p) \cap \Sigma$ may consist of infinitely

many curves; see Sections 3 and 4. To compute curves in $W^s(p) \cap \Sigma$, we consider the BVP defined by (3) subject to (4) or (5) and the additional boundary condition

$$G(\mathbf{u}(1)) = 0. \tag{7}$$

This BVP is well posed in the sense that a solution is given by a unique tuple $(\mathbf{u}, T)$, for each choice of δ in (4), or θ in (5). An initial solution can be found by monitoring (7) as a user-defined function in AUTO for fixed δ or θ during the continuation of an orbit segment in T. In fact, depending on the geometry of $W^s(p)$, several zeros of G may be found, and the corresponding solutions of the BVP can all be continued to yield different curves in $W^s(p) \cap \Sigma$. Continuation with T and δ (or T and θ) as continuation parameters yields a one-dimensional curve in $W^s(p) \cap \Sigma$. With the Python scripting option of AUTO it is possible to automate the generation and continuation of the corresponding BVPs.

The standard choice for the section is to consider a two-dimensional plane Σ, in which case G is simply a linear function; this is used in section 4. The BVP set-up above for finding curves in $W^s(p) \cap \Sigma$ is very similar to the ManBVP algorithm from [18] for the computation of one-dimensional stable and unstable manifolds of a periodic point of the associated Poincaré return map to the section Σ. The difference is that the invariant object of the vector field — the equilibrium — need not lie in the section Σ. As we will see in Section 3, it is sometimes convenient to consider a compact section, in this case a sphere $\Sigma = S$ around the saddle equilibrium (given by a nonlinear function G).

In either case, one faces the problem that the associated Poincaré return map is not a global diffeomorphism on the whole of Σ. In fact, the section is generically divided into open regions where the direction of the flow (measured with respect to the normal of the section) differs [42]. The boundary between these regions is formed by the tangency locus C, defined as the set of points where the flow of (1) is tangent to the section. The crucial observation is that the set $W^s(p) \cap \Sigma$ (or $W^s(p) \cap S$) may change even though the flow of the vector field remains topologically the same — we speak of a tangency bifurcation. Indeed, tangency bifurcations can be brought about simply by changing the section (for example, by moving Σ or changing the size of the sphere S), while the vector field remains unchanged [42]. It is, therefore, important not to confuse a tangency bifurcation of $W^s(p) \cap \Sigma$ (or $W^s(p) \cap S$) with a bifurcation of the vector field. In the present setting of vector fields in $\mathbb{R}^3$, when a single parameter is changed we may encounter generically the generation or disappearance of a closed intersection curve of $W^s(p)$ with the section (we also speak of a minimax transition of $W^s(p)$), and the local rearrangment of two different intersection curves (in a saddle transition of $W^s(p)$); see [42] for details.

2.2. **The manifold as a family of geodesic level sets.** Our second method for computing a stable manifold is based on the geometric idea that $W^s(p)$ can be viewed as a one-parameter family of geodesic level sets. This point of view is complementary to the one in Section 2.1 where $W^s(p)$ was represented as a one-parameter family of orbit segments. The advantage of representating $W^s(p)$ by geodesic level sets is that in this way one generates the 'most circular' mesh centered around the equilibrium p. Each geodesic level set has the property that the mesh points on it lie at the same geodesic distance from p; recall that the geodesic distance between two points is the arclength of the smallest path on the manifold that connects them.

We now briefly explain the GLS implementation [19] of the method [33, 34], which makes use of AUTO's collocation and pseudo-arclength continuation routine to find a solution family of an associated BVP in order to obtain a new mesh point. Indeed, a new geodesic level set — a closed one-dimensional curve in the setting of this paper — is computed point by point in this way, and the mesh is then extended by a triangulation of the band between the previous and the new geodesic level set. In other words, $W^s(p)$ is grown uniformly outwards from p by appropriate geodesic increments, which are determined by the local curvature of the manifold. While this method may seem somewhat cumbersome, the mesh it generates has very nice properties that can be used to understand the geometry of the computed manifold [36, 47, 48, 49].

The first approximate geodesic level set C_δ is simply given by K uniformly spaced mesh points on a circle with radius δ around p in the stable eigenspace $E^s(p)$. Suppose now that the algorithm has computed a mesh consisting of level sets C_δ up to a level set C_r. To find the geodesic level set C_b at a distance Δ from C_r we consider each of the mesh points r_k on C_r and determine associated (closest) points b_k on C_b. To this end, we construct a plane $\mathcal{F}_{r_k}$ (approximately) perpendicular to C_r at r_k. Then the sought after new point b_k lies on the (unknown, but locally well-defined) one-dimensional intersection curve $W^s(p) \cap \mathcal{F}_{r_k}$.

The idea is now to consider the solution family of the BVP given by (3) and the boundary conditions

$$\mathbf{u}(0) \in C_r, \tag{8}$$
$$\mathbf{u}(1) \in \mathcal{F}_{r_k}. \tag{9}$$

Here, C_r is represented by the piece-wise linear approximation through its mesh points. Starting from the trivial solution $\mathbf{u}(t) = r_k$, $0 \le t \le 1$ with $T = 0$, the GLS implementation calls AUTO's collocation and pseudo-arclength continuation routines to continue $\mathbf{u}$ in the parameter T (which is again negative since we compute a stable manifold). Notice that this BVP set-up at each mesh point is conceptually the same as in Section 2.1.1. During this computation we monitor the (Euclidean) distance

$$\Delta_T = \| \mathbf{u}(1) - r_k \|$$

between $\mathbf{u}(1)$ and r_k until a required small distance Δ is reached, which defines the new point b_k. To maintain a good resolution of the manifold, b_k is tested against accuracy criteria (involving the curvature along geodesics). In case b_k violates accuracy constraints, the geodesic level set currently being computed is discarded and Δ is reduced. Furthermore, mesh points may need to be added or removed during a computation; this is done in such a way that the global interpolation error remains bounded; see [19, 33, 34] for further details.

Figure 2 illustrates, with the example of a first piece of the Lorenz manifold $W^s(\mathbf{0})$ from Section 4, how the GLS method works in practice. Shown are all orbit segments (black curves) that were computed to find a next geodesic level set. Notice that the mesh points given by $\mathbf{u}(1)$ are quite uniformly spaced along the new geodesic level set, while the corresponding points $\mathbf{u}(0)$ of the orbit segments are condensed in places on the previous geodesic level set; this is particularly visible near the bottom of the vertical z-axis in Fig. 2. Also shown is how the overall mesh on $W^s(\mathbf{0})$ is built up, which requires adding mesh points as the manifold grows, for example, near the top of the vertical z-axis.

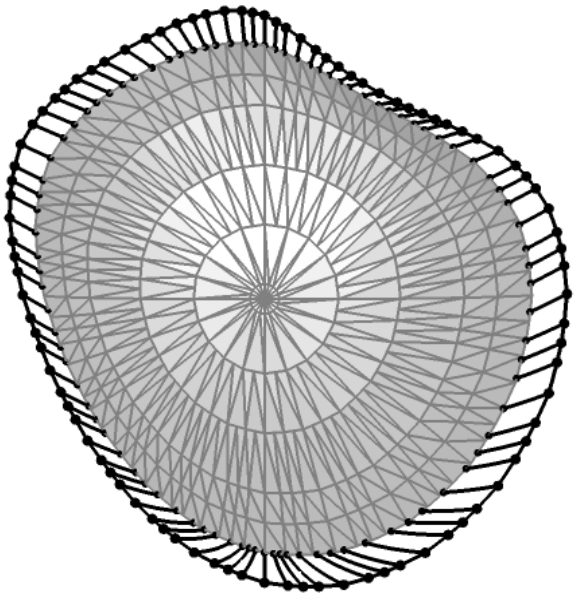

FIGURE 2. Illustration of the orbit segments computed by the GLS method to find the mesh points of the next geodesic level set; the data is for the Lorenz manifold with $\varrho = 10$.

3. **The stable manifold near a Shilnikov bifurcation.** A Shilnikov bifurcation [57, 58] refers to the occurence of a homoclinic orbit to a saddle-focus equilibrium p. Under suitable transversality conditions [30, 41, 59], this global bifurcation is of codimension one, meaning that it occurs generically at an isolated parameter value λ^* in a one-parameter family of vector fields.

Without loss of generality we suppose here that $Df(p)$ has a pair of complex conjugate eigenvalues $\lambda^s_{1,2} = \rho \pm \eta i$ with $\rho < 0$ and $\eta \neq 0$ and a real eigenvalue $\lambda^u > 0$, so that the saddle-focus has a two-dimensional stable manifold $W^s(p)$ and a one-dimensional unstable manifold $W^u(p)$. A Shilnikov homoclinic orbit is then formed at λ^* by the branch of $W^s(p)$ that lies in $W^u(p)$.

The unfolding of the Shilnikov bifurcation (that one obtains when the parameter λ is varied from λ^*) depends on the sign of the saddle quantity $\sigma = \lambda^u + \rho$. For $\sigma < 0$ a unique and stable limit cycle Γ bifurcates from the homoclinic orbit; one speaks of a *simple Shilnikov bifurcation*. For $\sigma > 0$, on the other hand, the unfolding features infinitely many periodic orbits of saddle type in a tubular neighborhood of the homoclinic orbit to the saddle-focus; this case is also known as a *chaotic Shilnikov bifurcation*. The proof by Shilnikov in the 1960s of the existence of an invariant horseshoe in the return map near this global bifurcation is a celebrated and now classical result in dynamical systems [57, 58].

3.1. **Shilnikov bifurcations in a laser model.** As is the case for any global bifurcation, a normal form vector field for the Shilnikov bifurcation does not exist. On the other hand, Shilnikov bifurcations occur naturally in many applications, for example, in nerve impulse propagation [20], electro-chemical reactions [4] and

oxidation processes [45], electrodynamic convection in liquid crystals [52], and food chain models [9], to name just a few.

Another important class of systems where one finds Shilnikov bifurcations are models of laser systems [65, 66, 68], and we consider here the specific example of a semiconductor laser with optically injected light from a second laser. This system is an example of an externally driven (optical) oscillator, and it can be modeled by the so-called rate equations

$$\begin{cases} \dot{E} &= K + \left(\frac{1}{2}(1+i\alpha)n - i\omega\right) E, \\ \dot{n} &= -2Gn - (1+2Bn)(|E|^2 - 1) \end{cases} \tag{10}$$

for the complex electric field $E = E_x + E_y\, i$ and the population inversion n (the number of electron-hole pairs that may recombine to produce a photon); see [66, 68] for more details. The main parameters are the amplitude K and the detuning ω (the difference between the frequencies of laser and injected light). Throughout, we keep K fixed at $K = 0.45$; furthermore, B, G and α describe material properties of the laser and, for our purposes, they are fixed at $B = 0.015$, $G = 0.035$, $\alpha = 2$.

An extensive bifurcation analysis in [65, 68] of system (10) revealed, among other dynamical features, many curves of Shilnikov bifurcations to a saddle-focus p. In particular, it was found that a simple Shilnikov bifurcation near a curve of saddle-node bifurcations of p gives rise to excitability; see also [38]. More specifically, in the parameter region in question there is a unique attracting equilibrium q near p. A perturbation of the system past the stable manifold $W^s(p)$ results in a large excursion in phase space. The system then settles back to the attractor q, and it can be excited again. Physically, the laser produces a pulse of light in reaction to a small perturbation. In other words, $W^s(p)$ acts as the excitability threshold of the system, and the exact shape of the pulse is determined by the shape of the nearby saddle-focus homoclinic orbit. In fact, bifurcation analysis showed that the injection laser may show a multi-pulse response to a single perturbation [67] (in the vicinity of n-homoclinic orbits), and this was later confirmed experimentally [23, 63].

3.2. **The simple Shilnikov bifurcation.** Our aim is to investigate how the geometry of the two-dimensional stable manifold changes during a simple Shilnikov bifurcation (of a 1-homoclinic orbit), and the laser model (10) is used here simply as a concrete and convenient example vector field that features this bifurcation. More specifically, we consider the Shilnikov homoclinic orbit of the saddle-focus $p \approx (0.728926, 0.7165664, -0.627905)$ that one finds (for example, with HomCont) at $\omega \approx -0.93653321169$; the eigenvalues of p at the bifurcation are $\lambda^u = 0.205017$ and $\lambda^s_{1,2} = -0.452133 \pm 1.11566\, i$, so $\sigma = -0.247116$ and we are indeed dealing with a simple Shilnikov bifurcation. This global bifurcation is unfolded here by changing the detuning ω.

Figure 3 shows the one-dimensional unstable manifold $W^u(p)$ before, at and after the bifurcation; also shown is a small disc in the stable linear eigenspace $E^s(p)$. One of the two branches of $W^u(p)$ is quite short and always converges directly to the attracting equilibrium $q \approx (1.01442, 0.180927, -0, 859854)$. By contrast, the branch of $W^u(p)$ on the other side of $E^s(p)$ makes a large excursion before returning to a neighborhood of the saddle-focus p. In Fig. 3(a) this branch 'dives under' $E^s(p)$ [see panel (a2)] so that it also ends up at the attractor q. In this situation the system is excitable: any perturbation from the attractor q sufficiently past the saddle p will lead to a global excursion that follows the longer branch of $W^u(p)$. Figure 3(b)

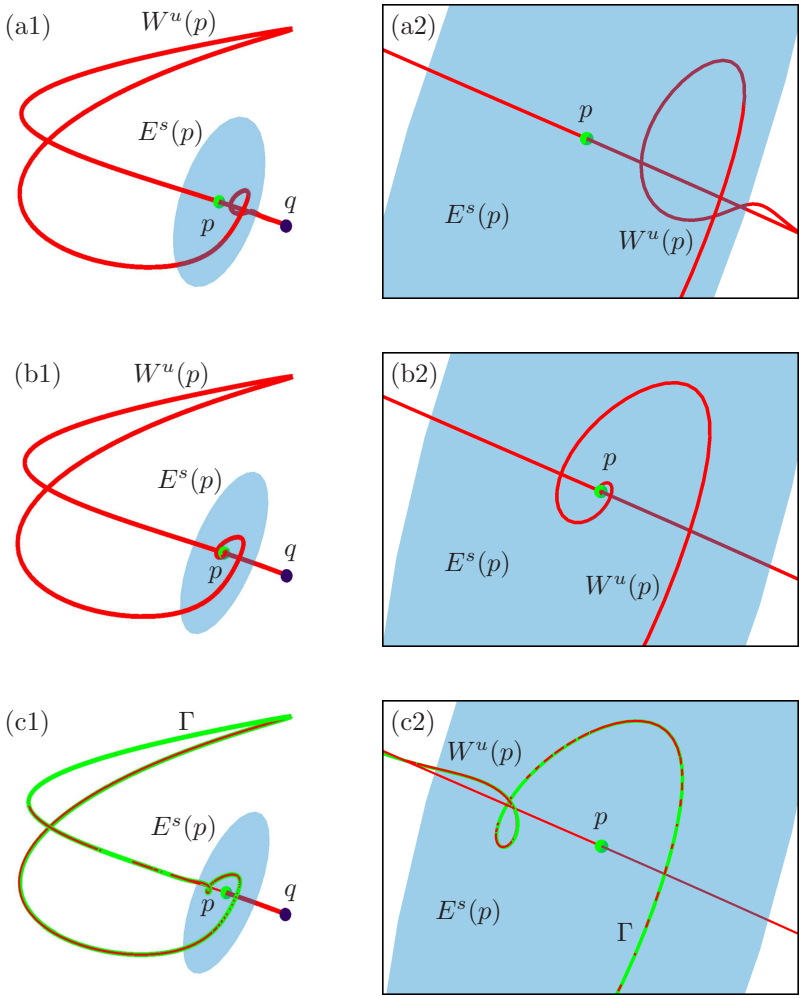

FIGURE 3. The unstable manifold $W^u(p)$ and a small disc representing the stable eigenspace $E^s(p)$ before, at and after a simple Shilnikov bifurcation of the laser model (10). The right column shows enlargements near the saddle-focus p; $\omega = -0.93$ in row (a), $\omega \approx -0.93653321169$ in row (b), and $\omega = -0.94$ in row (c).

shows the Shilnikov homoclinic orbit at the moment of bifurcation, when the longer branch of $W^u(p)$ spirals into the saddle focus p. Figure 3(c) shows the situation past the Shilnikov bifurcation. The longer branch of $W^u(p)$ now stays on the same side of $E^s(p)$ and accumulates on an attracting periodic orbit Γ. Note that we are showing a situation quite close to the Shilnikov bifurcation, so that Γ passes very close to p (and it has the quite large period $T_\Gamma \approx 19.7378$); see panel (c2).

Figure 3 presents the simple Shilnikov bifurcation in the spirit of 'classical sketches' of $W^u(p)$, as they can be found in textbooks [25, 41, 59]. It forms the starting point for our investigation into the properties of the two-dimensional stable manifold $W^s(p)$. In fact, until now very little is known about the geometry of $W^s(p)$ at the

Shilnikov bifurcation, and images such as Fig. 3 only give a vague idea of what $W^s(p)$ looks like. For instance, if we imagine the two-dimensional manifold $W^s(p)$ at the homoclinic bifurcation growing backwards in time from the saddle-focus p, it is clear that it consists initially of trajectories that spiral around p. Yet it is not obvious at all how this growth process continues once $W^s(p)$ has left a neighborhood of p. The only thing that we can assert is that a part of the manifold $W^s(p)$ near the homoclinic orbit must head back towards p. In the process, the rotational component of the vector field near the saddle-focus must induce twisting of $W^s(p)$.

Questions that remain are: what is the global shape of $W^s(p)$ near a simple Shilnikov bifurcation? How does $W^s(p)$ 'return' to the equilibrium p? How does the topological change due to this Shilnikov bifurcation manifest itself in terms of the geometry of $W^s(p)$? And how does this lead to the creation of the basin of the bifurcating attracting periodic orbit Γ?

3.2.1. *The geometry of $W^s(p)$ in phase space.* Figure 4 shows a global view of the stable manifold $W^s(p)$, before and after the simple Shilnikov bifurcation of (10) at $\omega \approx -0.93653321169$. The manifold has been computed with the method in Sec. 2.1.1. More specifically, we continued orbit segments of fixed integration time $T_0 = 40$ whose end point $\mathbf{u}(0)$ satisfies (4) where $\delta \in [1 \times 10^{-5}, 1.15 \times 10^{-4})$ with $\omega = -0.93$ before the bifurcation in Fig. 4(a), and $\delta \in [1 \times 10^{-5}, 7 \times 10^{-5})$ with $\omega = -0.94$ after the bifurcation in Fig. 4(b). For ease of reference, all images in Fig. 4 are shown from the same viewpoint as those in Fig. 3. In each row, two styles of rendering show the same manifold as a solid surface and as a transparent surface, respectively. Figure 4 gives a good impression of the overall shape of $W^s(p)$, but it does not illustrate very well where $W^s(p)$ lies in relation to the unstable manifold $W^u(p)$ and the saddle-focus p. The transparent rendering is helpful in that it shows how $W^s(p)$ folds and twists as it grows away from the saddle focus p. In the process several layers of $W^s(p)$ are formed that are 'hidden' inside an 'external shell'; note that some layers of $W^s(p)$ even 'surround' the attractor q. Overall, Fig. 4 presents global images of a two-dimensional invariant manifold near a Shilnikov bifurcation for the first time in great accuracy and detail. The manifold $W^s(p)$ emerges as an intriguing two-dimensional surface that changes with ω, but it is not yet clear what the exact nature of this change actually is.

To address this issue we first consider the geometry of $W^s(p)$ in a tubular neighborhood around the homoclinic orbit. Figure 5 shows only a thin strip of $W^s(p)$ near the homoclinic orbit; the situations before, at and after the simple Shilnikov bifurcation are exactly as shown in Fig. 3. Each strip has been computed with the method in Sec. 2.1.3 as orbit segments that end (after one global excursion) on the sphere $S = S_{0.5}(p)$ of radius 0.5 around the saddle-focus p; hence, $\Sigma = S_{0.5}(p)$ is defined by $G(\mathbf{u}(1)) = \|\mathbf{u}(1) - p\| - 0.5 = 0$. The strip starts near p, where it is very thin, and it becomes wider as it returns to a neighborhood of the saddle-focus p. The strip, and hence the stable manifold $W^s(p)$, is forced to rotate around $W^u(p)$ when it returns; see the enlargements near p in Fig. 5. Notice from the right column of the figure that, as a result of the bifurcation, the unstable manifold $W^u(p)$ moves to the other side of the shown strip of $W^s(p)$. At the moment of the Shilnikov bifurcation $W^s(p)$ forms several layers that accumulate on each other in the vicinity of p; see Fig. 5(b). Notice further that after the bifurcation, in Fig. 5(c), the strip moves upwards again.

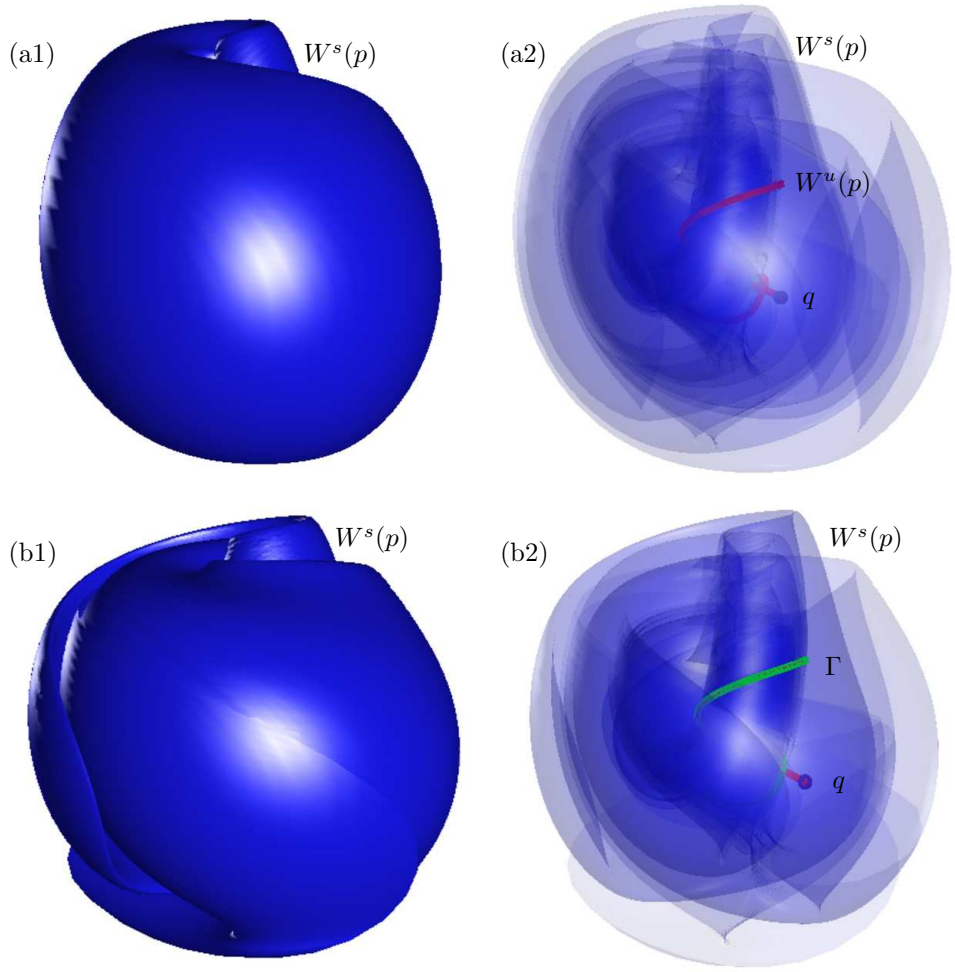

FIGURE 4. The stable manifold $W^s(p)$, computed via the continuation of orbit segments of fixed period $T_0 = 40$, with $\omega = -0.93$ before (a), and with $\omega = -0.94$ after the simple Shilnikov bifurcation (b). The viewpoint is the same as in the left column of Fig. 3; the manifold is rendered both as a solid surface (left column) and as a transparent surface (right column).

3.2.2. *Intersection of $W^s(p)$ with a sphere.* While Fig. 5 shows the rotational behavior of $W^s(p)$ near p very clearly, the exact nature of the topological change of the dynamics during the simple Shilnikov bifurcation remains somewhat nebulous. To study how the associated geometric change of $W^s(p)$ gives rise to the basin of the attracting periodic orbit Γ, we now consider the intersection curves of $W^s(p)$ with the sphere $S = S_{0.5}(p)$. Figure 6(a) shows how S sits inside the shell-like structure of the entire manifold $W^s(p)$ before the Shilnikov bifurcation. (Here $W^s(p)$ is shown from the opposite side compared to Fig. 4.) As Fig. 6(b) shows, only a small strip of $W^s(p)$ near $W^u(p)$ returns to S (provided that S is sufficiently small).

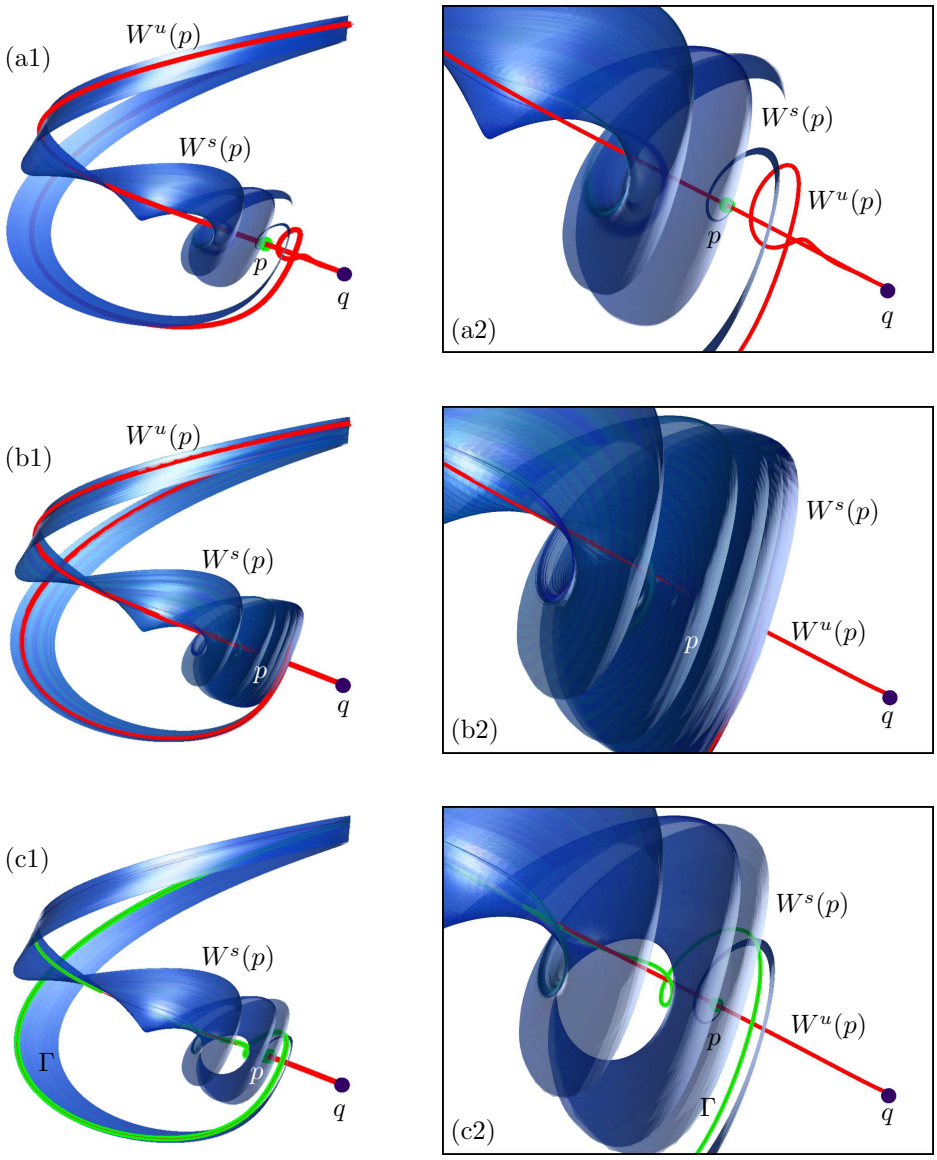

FIGURE 5. A strip of the stable manifold $W^s(p)$ that returns to a neighborhood of p, before, at and after a simple Shilnikov bifurcation of the laser model (10). Viewpoint, enlargements and parameter values are as in Fig. 3.

The question is now how $W^s(p) \cap S$ changes during the simple Shilnikov bifurcation, and how this results in a topological change of the dynamics. The intersection of $W^s(p)$ and a given sphere may consist of many curves (depending on the size of the sphere), but it suffices to consider only the two curves $W^s_0 \cup W^s_1 \subseteq W^s(p) \cap S$ that are shown in Fig. 7. Here W^s_0 is the intersection of $W^s_{\rm loc}(p)$ with S, and W^s_1 is the curve that corresponds to the first return of $W^s(p)$ to S along the unstable

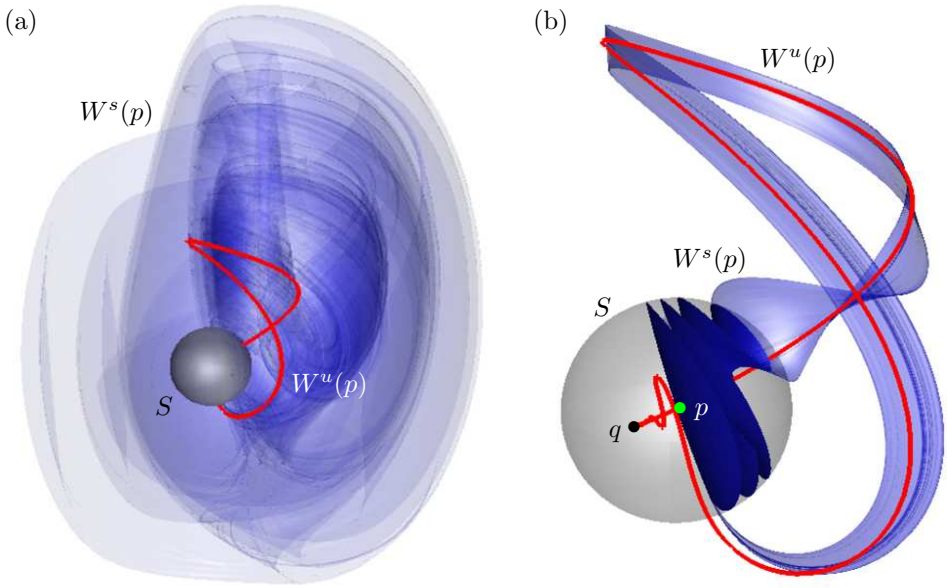

FIGURE 6. Intersections of $W^s(p)$ with the sphere $S = S_{0.5}(p)$ before the Shilnikov bifurcation. Panel (a) shows how S sits inside the manifold; only a thin strip of $W^s(p)$ returns to the sphere after following the upper branch of $W^u(p)$ (b).

manifold $W^u(p)$. Note that W^s_0 is a closed curve that divides S into two parts. The left column of Fig. 7 shows the curves W^s_0 and W^s_1 on the sphere S in phase space, together with the unstable manifold $W^u(p)$; compare with Figs. 3 and 5. The right column of Fig. 7 shows $W^s(p) \cap S$ in convenient spherical polar coordinates on S, given by

$$\left\{ \begin{array}{rcl} E_x(\theta,\varphi) & = & p_x + R\cos(2\pi\theta)\sin\left(\pi(1-\varphi)\right), \\ E_y(\theta,\varphi) & = & p_y + R\sin(2\pi\theta)\sin\left(\pi(1-\varphi)\right), \\ n(\theta,\varphi) & = & p_z + R\cos\left(\pi(1-\varphi)\right), \end{array} \right. \tag{11}$$

where $p = (p_x, p_y, p_z)$ and $R = 0.5$ is the radius of S. The cylindrical chart $\{(\theta,\varphi) : 0 \le \theta \le 1, 0 < \varphi < 1\}$ is a diffeomorphic image of the sphere, except at the 'north pole' and the 'south pole' of S (corresponding to $\varphi = 1$ and $\varphi = 0$, respectively). However, the poles do not cause a problem since the manifolds under consideration stay away from them throughout the Shilnikov bifurcation. Hence, the charts in Fig. 7 are a convenient representation of $W^s(p) \cap S$ on the whole of the sphere S.

Also shown in Fig. 7 is the tangency locus $C \subset S$, where the flow of the vector field (10) is tangent to the sphere S. It can be computed as the set of points $(c_x, c_y, c_z) \in S$ that satisfy

$$(c_x - p_x)\dot{E}_x + (c_y - p_y)\dot{E}_y + (c_z - p_z)\dot{n} \;=\; 0, \tag{12}$$

where $(\dot{E}_x, \dot{E}_y, \dot{n})$ is given by the right-hand side of (10) evaluated at (c_x, c_y, c_z). The existence of $C \neq \emptyset$ implies that the first-return map to S is not a diffeomorphism on the whole of S [42]. In the present setting, the relevance of C, which consists

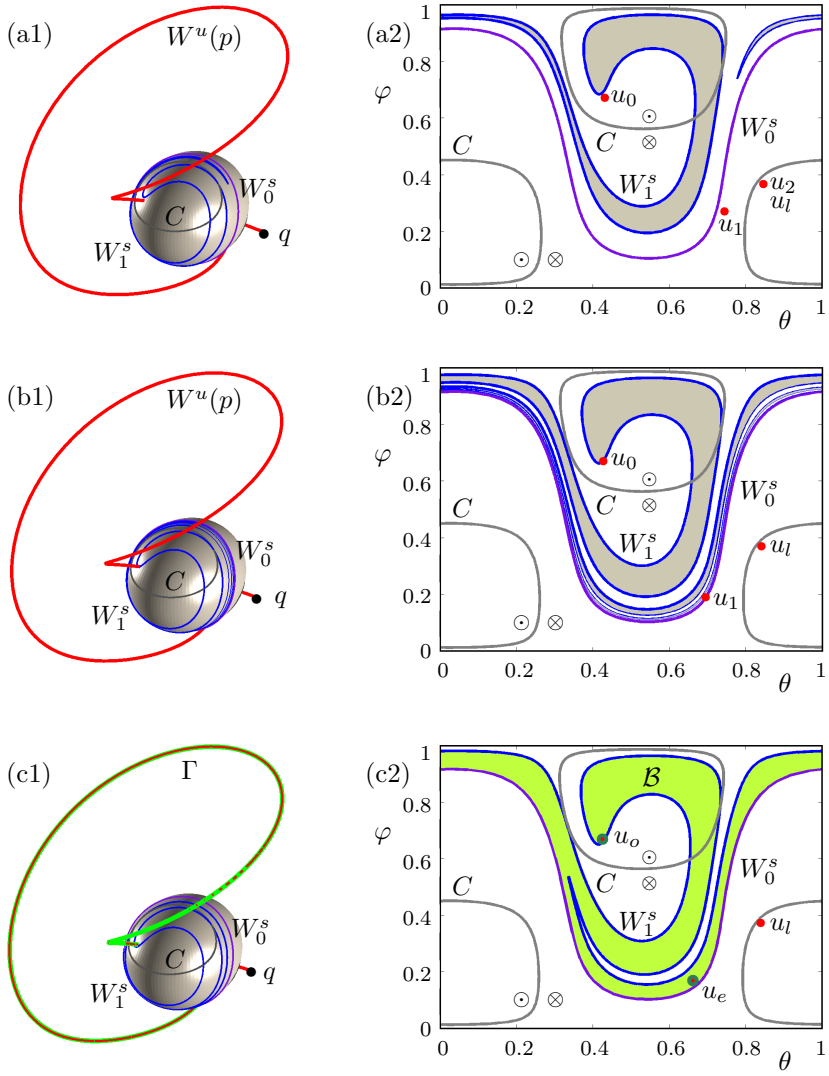

FIGURE 7. The set $W^s(p) \cap S$ before, at and after the simple Shilnikov bifurcation. The left column shows the sphere $S = S_{0.5}(p)$ in phase space together with $W^u(p)$, and the right column shows the cylindrical chart given by (11). Parameters are as in Fig. 3.

of two closed curves, is that it divides S into two regions where the flow points out of the sphere (indicated by the symbol $\odot$) and a single region where the flow points into the sphere (indicated by the symbol $\otimes$). Notice that the two intersection points of the periodic orbit Γ in Fig. 7(c) must necessarily lie in the two different regions. Furthermore, the curve W_1^s crosses C. This is a generic property of two-dimensional global manifolds that we will also encounter in Sec. 4. We remark that

the corresponding one-dimensional intersection curves can be computed reliably even when they cross C; see also [18].

We now discuss the geometry of W^s before, at and after the Shilnikov bifurcation in more detail. The lower branch of the unstable manifold $W^u(p)$ goes to the attractor q and, hence, has a single intersection u_l with S throughout. Before the bifurcation, in row (a) of Fig. 7, the upper branch of $W^u(p)$ intersects S first in the point u_0. (Note that $W^u_{\rm loc}(p) \cap S = \{u_l, u_0\}$.) This branch of $W^u(p)$ returns to enter S below the curve W^s_0 at u_2 and then exits again at the point u_3 (which is indistinguishable from u_l) to end up at the attractor q as well. The curve W^s_1 bounds a region of S [shaded in Fig. 7(a2)] that does not contain the point u_0. At the Shilnikov bifurcation, in row (b) of Fig. 7, W^s_1 and the shaded region it bounds accumulate on W^s_0. The upper branch of $W^u(p)$ forms the homoclinic orbit, which means that $W^u(p) \cap S = \{u_0, u_1\}$ and these two points lie on W^s_1 and W^s_0, respectively. After the bifurcation, in row (c) of Fig. 7, there is an attracting periodic orbit Γ whose basin of attraction $\mathcal{B}$ on S is bounded by both W^s_1 and W^s_0; the basin of attraction of q is the interior of the complement of $\mathcal{B}$. Furthermore, now $W^u(p) \cap S = \{u_0, u_1, \cdots\}$ consists of infinitely many points that all lie above W^s_0 and very rapidly converge to $\Gamma \cap S$; in Fig. 7(c2) the (indistinguishable) odd-numbered intersection points are indicated by the symbol u_o and the (equally indistinguishable) even-numbered ones by u_e. We can summarize our findings as follows.

Result. (simple Shilnikov bifurcation)

Consider a sufficiently small sphere S around a saddle-focus equilibrium p with negative saddle quantity near a simple Shilnikov bifurcation.

(S1) The basin $\mathcal{B} \subset S$ of the bifurcating attracting periodic orbit Γ is bounded by the two curves W^s_0 and W^s_1 of first and second return of $W^u(p)$ to S. It is a large region of S that can be identified as the continuation of the region bounded only by W^s_1 before the Shilnikov bifurcation.

(S2) As the bifurcation is reached from either direction of the parameter, the curve W^s_1 accumulates onto W^s_0.

The accumulation process of W^s_1 onto W^s_0 as the simple Shilnikov bifurcation is approached is illustrated further in Fig. 8. Before the Shilnikov bifurcation, the shaded region bounded by W^s_1 develops a growing 'tail' that accumulates on W^s_0 as the bifurcation is approached (ω is decreased); see the sequence Fig. 7(a2), Fig. 8(a1) and (a2). After the Shilnikov bifurcation, on the other hand, the non-shaded region bounded by W^s_1 forms a 'tail' as the bifurcation is approached (ω is increased). This means, that a small narrow and growing 'inlet' is taken out of the basin $\mathcal{B}$ of Γ; see the sequence Fig. 7(c2), Fig. 8(b2) and (b1). Both convergence processes have the same limit that is shown in Fig. 7(b2).

4. **The Lorenz manifold near the homoclinic explosion.** The well-known Lorenz equations [44] are given as the vector field

$$\left\{ \begin{array}{rcl} \dot{x} &=& \sigma(y-x), \\ \dot{y} &=& \varrho x - y - xz, \\ \dot{z} &=& xy - \beta z. \end{array} \right. \tag{13}$$

The system describes a simplified model for convection, which is non-dimensionalized so that the onset of convection occurs at the (rescaled) Rayleigh number $\varrho = 1$. Lorenz used the values $\sigma = 10$, $\beta = 8/3$ and $\varrho = 28$ to find and explain sensitive

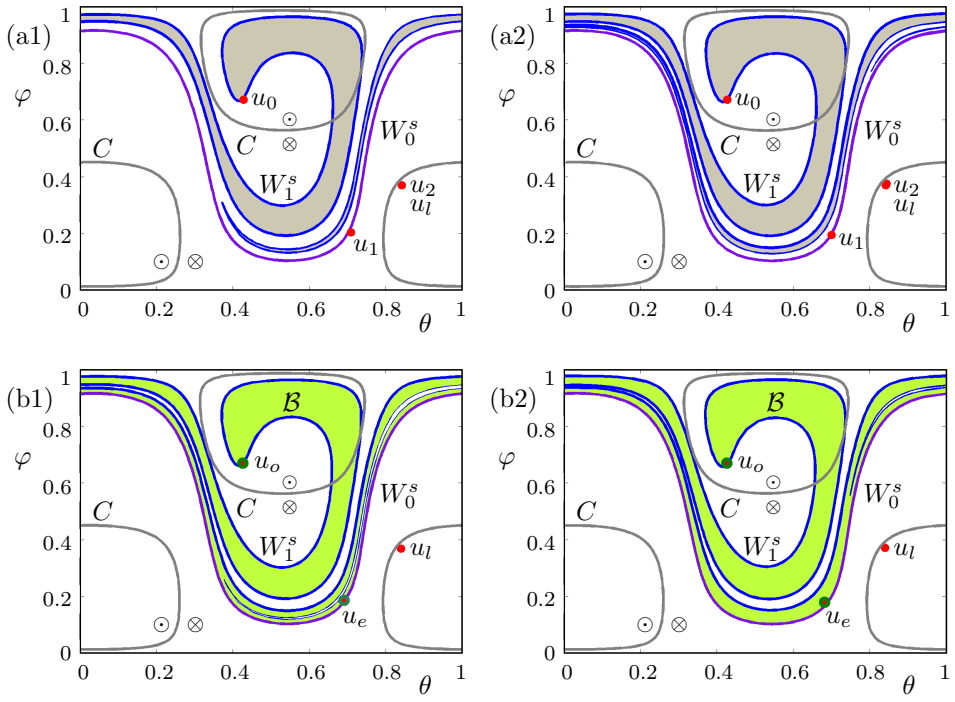

FIGURE 8. Illustration of the accumulation of W_1^s onto W_0^s as the Shilnikov bifurcation at $\omega \approx -0.93653321169$ is approached; panels (a1) and (a2) are for $\omega = -0.935$ and $\omega = -0.936$ (before the bifurcation), and panels (b1) and (b2) are for $\omega = -0.937$ and $\omega = -0.938$ (after the bifurcation).

dependence on the initial conditions in (13). We keep σ and β fixed at these values, and will focus on how the dynamics depends on the parameter ϱ.

The Lorenz equations (13) have at most three equilibria. The origin $\mathbf{0}$ is always an equilibrium, and two further equilibria

$$p^{\pm} = (\pm\sqrt{\beta(\varrho-1)}, \pm\sqrt{\beta(\varrho-1)}, \varrho-1)$$

exist only when $\varrho > 1$. More specifically, the origin is stable for $\varrho < 1$ and loses its stability at $\varrho = 1$ in a bifurcation, in fact, in a pitchfork bifurcation due to the invariance of (13) under the transformation $(x, y, z) \mapsto (-x, -y, z)$, which is physically a rotation over π about the z-axis. For $\varrho > 1$ the origin is a saddle with one unstable and two stable eigenvalues. The two (symmetrically related) equilibria $p^{\pm}$ that emerge from the pitchfork bifurcation are initially stable and correspond to convection dynamics.

4.1. **The homoclinic explosion point.** Our interest here is in a dramatic global bifurcation of the Lorenz system — called a homoclinic explosion point — that occurs at $\varrho = \varrho_{\text{hom}} \approx 13.9162$. At this value of ϱ one finds a symmetric pair of homoclinic orbits, which unfold to create a symmetric pair of primary saddle periodic orbits $\Gamma^{\pm}$ for $\varrho > \varrho_{\text{hom}}$; see Fig. 9. What is more, this global bifurcation is responsible for the birth of all chaotic dynamics in the Lorenz system, hence the

name [60]. Indeed, it creates many more saddle periodic and also homoclinic orbits in a tubular neighborhood of the two homoclinic orbits. This chaotic dynamics is initially unstable [22, 60], but gives rise to chaotic transients of trajectories, which all end up at either of the two attractors $p^{\pm}$ — one speaks of the preturbulent regime [31, 69]. For completeness, we briefly mention how the transition to the Lorenz attractor for $\varrho = 28$ continues. The preturbulent regime ends when the chaotic dynamics becomes attracting. This happens at $\varrho = \varrho_{\rm het} \approx 24.0579$ where one finds a symmetric pair of heteroclinic connections of $W^u(\mathbf{0})$ from $\mathbf{0}$ to $\Gamma^{\pm}$. The ensuing chaotic attractor co-exists with the two attractors $p^{\pm}$ until the latter become saddle equilibria in a subcritical Hopf bifurcation at $\varrho_H = \frac{470}{19} \approx 24.736842$, where the primary saddle periodic orbits $\Gamma^{\pm}$ disappear. For further details and, in particular, other homoclinic bifurcation points in the Lorenz equations, see [15] and references therein.

The homoclinic explosion at $\varrho = \varrho_{\rm hom}$ has been illustrated generally only in terms of one-dimensional objects: both branches of the one-dimensional unstable manifold $W^u(\mathbf{0})$ lie in the two-dimensional stable manifold $W^s(\mathbf{0})$ to form the pair of homoclinic orbits that connect $\mathbf{0}$ back to itself. In the process the two periodic orbits $\Gamma^{\pm}$ (which are also one-dimensional objects) are born. The homoclinic explosion is illustrated in Figure 9 by a three-dimensional view of the equilibria and $W^u(\mathbf{0})$ along with the one-dimensional strong stable manifolds $W^{ss}(p^{\pm})$ of $p^{\pm}$; also shown for orientation is a small disc in the two-dimensional stable eigenplane $E^s(\mathbf{0})$ of the origin. Panel (a) shows the situation before the homoclinic bifurcation; here $\varrho = 10$, which is representative for all $1 < \varrho < \varrho_{\rm hom}$. The left and right branches of $W^u(\mathbf{0})$ converge to p^- and p^+, respectively, in a spiralling manner by rotating around the one-dimensional strong stable manifolds $W^{ss}(p^{\pm})$. Figure 9(b) shows the actual homoclinic bifurcation at $\varrho = \varrho_{\rm hom}$. Instead of converging to $p^{\pm}$ the two branches of $W^u(\mathbf{0})$ come back to $\mathbf{0}$ and are tangent to the stable eigenplane $E^s(\mathbf{0})$. The situation after the homoclinic bifurcation is shown in Fig. 9(c) for $\varrho = 20$, which is representative for ϱ-values in the preturbulent regime. Note that the two branches of $W^u(\mathbf{0})$ again converge to $p^{\pm}$, but the branch that converged to p^- before the bifurcation now converges to p^+, and vice versa. Furthermore, we now have a pair $\Gamma^{\pm}$ of primary saddle periodic orbits.

4.2. **The geometry of $W^s(\mathbf{0})$ in phase space.** We consider here in detail what happens to the two-dimensional stable manifold $W^s(\mathbf{0})$ — which we also refer to as the *Lorenz manifold* — during the transition from stable convection to the preturbulent regime in the homoclinic explosion at $\varrho_{\rm hom}$. This work follows on from our previous work in [15], where we considered bifurcations of heteroclinic connections from $p^{\pm}$ to $\mathbf{0}$, that is, how the intersections of $W^s(\mathbf{0})$ and $W^u(p^{\pm})$ change with ϱ. Clearly, the phase portraits on the level of one-dimensional objects in Fig. 9(a) and (c) are topologically different, but it is not clear at all from these images what this global bifurcation means for $W^s(\mathbf{0})$ and how preturbulence arises in the phase space at large. More specifically, the situation is this. Before and after the homoclinic explosion the two equilibria $p^{\pm}$ are the only attractors and, hence, the union of their basins remains dense in $\mathbb{R}^3$. Nevertheless, there must be a topological change of the two basins at the homoclinic explosion that generates the possibility of arbitrarily long transients for $\varrho > \varrho_{\rm hom}$. Since the Lorenz manifold $W^s(\mathbf{0})$ forms a basin boundary, the issue is to find out how it changes globally at $\varrho_{\rm hom}$. To this end, we employ the numerical methods from Sec. 2 to compute $W^s(\mathbf{0})$ in different ways to understand and illustrate its complicated geometry. We remark that our

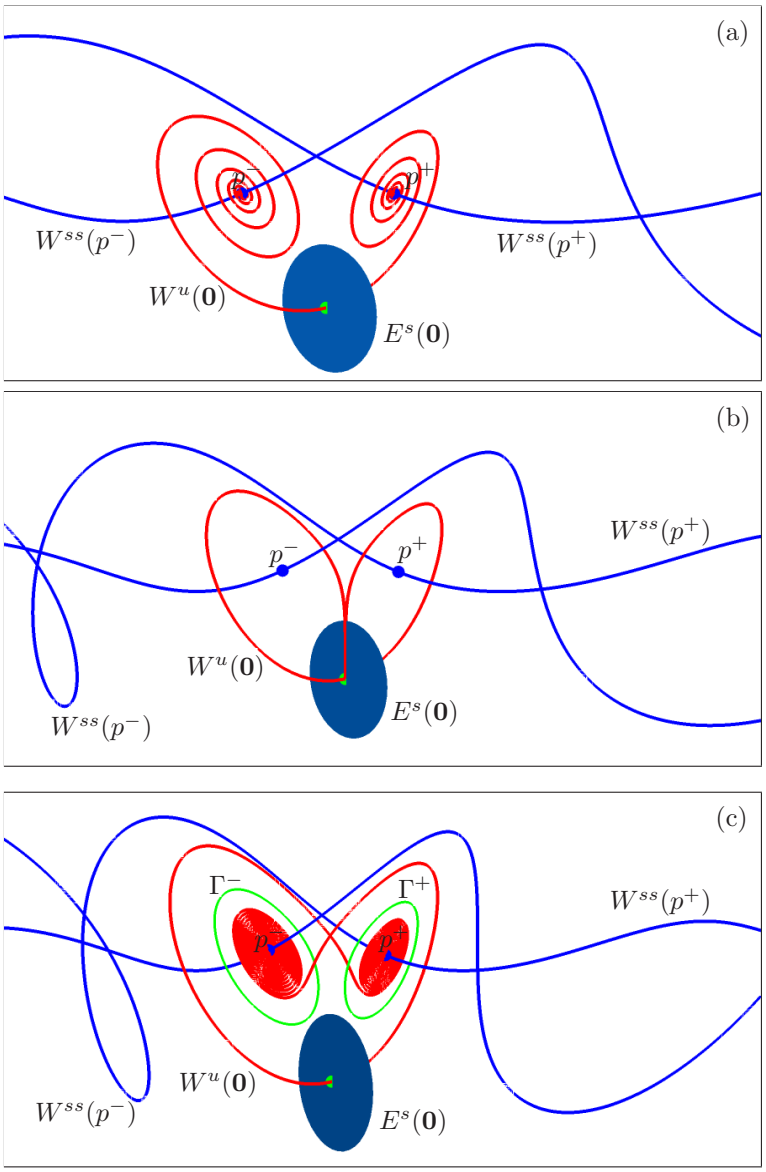

FIGURE 9. The homoclinic bifurcation at $\varrho = \varrho_{\text{hom}} \approx 13.9162$ is well understood on the level of the one-dimensional manifolds. Shown here are the equilibria $\mathbf{0}$ and $p^{\pm}$ with the one-dimensional manifolds $W^u(\mathbf{0})$ and $W^{ss}(p^{\pm})$, and a small disc representing $E^s(\mathbf{0})$. Panel (a) is for $\varrho = 10$, panel (b) is at the bifurcation, and panel (c) is for $\varrho = 20$; also shown in (c) are the bifurcating periodic orbits $\Gamma^{\pm}$. In all panels the z-axis is the vertical axis and the view is along the direction rotated by $\pi/30$ with respect to the x-axis.

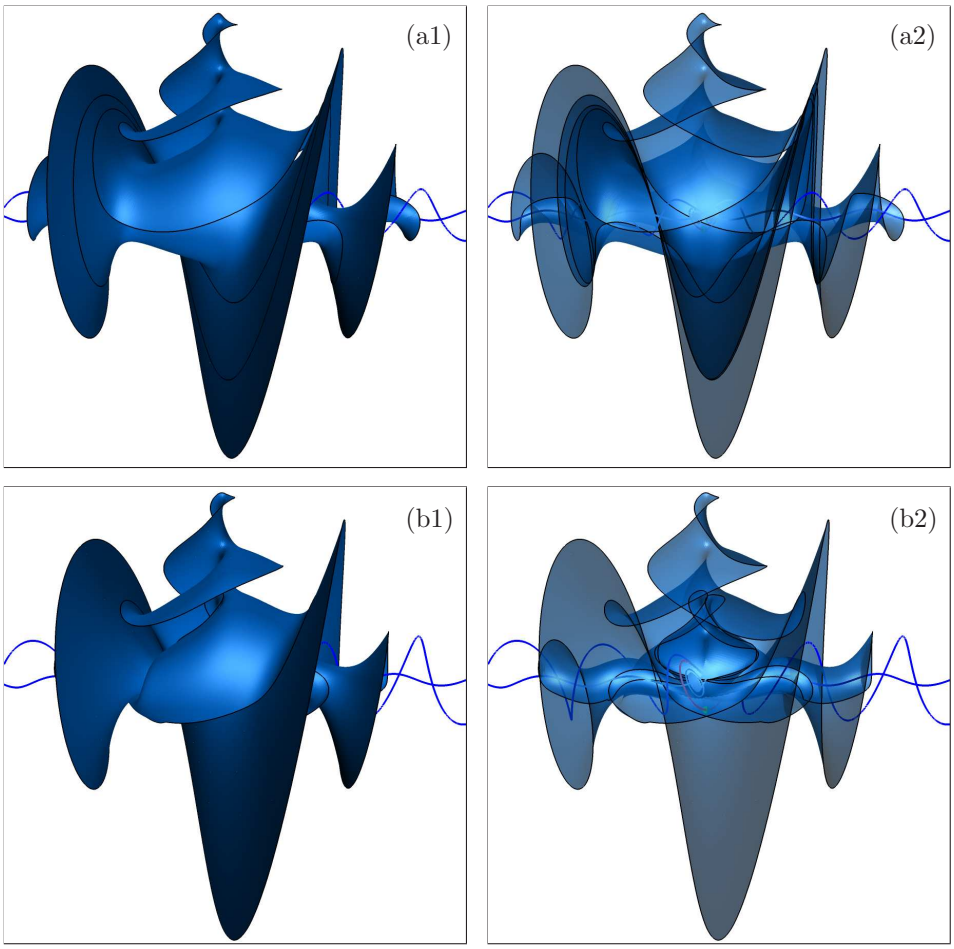

FIGURE 10. The Lorenz manifold for $\varrho = 10$ (a) and for $\varrho = 20$ (b), computed with the method from Sec. 2.2 up to geodesic distance 150 and 148.75, respectively. The manifold is rendered as a solid surface in the left column and as a transparent surface in the right column; the bounding last geodesic level sets are drawn as black curves; also shown are the one-dimensional objects from Fig. 9.

results can be seen as extending the work of Perelló in [53], whose three hand-drawn sketches were the first and, to our knowledge, the only attempts to date of illustrating the geometry of $W^s(\mathbf{0})$ as a surface through the homoclinic explosion. Note that Perelló's sketch for $\varrho = 28$ also formed the basis for the illustrations by Abraham and Shaw [1]; see also [15, 47].

Figure 10 shows the Lorenz manifold $W^s(\mathbf{0})$ before and after the homoclinic bifurcation, together with the one-dimensional objects from Fig. 9(a) and (c). The last geodesic level set (at geodesic distance 150 and 148.75, respectively) has been drawn as a closed black curve to help interpret how $W^s(\mathbf{0})$ changes in the homoclinic bifurcation at ϱ_{hom}. Observe from Fig. 10(a) that the shown part of $W^s(\mathbf{0})$ for

$\varrho = 10$ has several layers in the region near the negative z-axis. For $\varrho = 20$, on the other hand, these are absent and $W^s(\mathbf{0})$ appears to 'roll up' in the region of positive z.

Our goal is now to understand this geometric change of $W^s(\mathbf{0})$ and its consequences for the dynamics of the Lorenz system in more detail. To this end, we study one-dimensional intersections of $W^s(\mathbf{0})$ with the section $\Sigma_\varrho = \{z = \varrho - 1\}$, that is, the horizontal plane through the equilibria $p^\pm$. This section is the standard choice that has been used to study the dynamics on the Lorenz attractor by means of a local Poincaré map. Such studies consider only a neighborhood of the intersection of the chaotic attractor with Σ_ϱ where the flow is transverse to the section, so that the Poincaré map, defined as the return to this neighborhood, is a local diffeomorphism [25, 60]. By contrast, we consider here the intersection set $W^s(\mathbf{0}) \cap \Sigma_\varrho$, which is a much larger object that necessarily interacts with the locus C where the flow is tangent to Σ_ϱ [42]. It is straighforward to see that

$$C = \{(x, y) \mid y = \beta(\varrho - 1)/x\}\,.$$

Hence, the tangency locus C consists of two (symmetrically related) hyperbolas that divide Σ_ϱ into two outer regions where the directed flow of (13) points up (in the direction of positive z), indicated by $\odot$, and a central region where the flow points down (in the direction of negative z), indicated by $\otimes$. Notice that the equilibria, which lie in Σ_ϱ by its choice, must and do indeed lie on C. The location of the intersection curves in $W^s(\mathbf{0}) \cap \Sigma_\varrho$ relative to C provides information about the dynamics on $W^s(\mathbf{0})$; namely, one can deduce how intersection curves map to each other under the global Poincaré map, which is defined as the first-return map on the entire section Σ_ϱ.

4.3. **Intersection of $W^s(\mathbf{0})$ with Σ_ϱ for $\varrho = 10$.** Figure 11 illustrates for $\varrho = 10$ how intersection curves of $W^s(\mathbf{0})$ with Σ_ϱ arise; here we take advantage of the fact that our numerical method grows this surface as a sequence of geodesic level sets. Also shown in the figure are the one-dimensional manifolds $W^u(\mathbf{0})$ and $W^{ss}(p^\pm)$; they intersect Σ_ϱ in a sequence of points that lie alternatingly on one side of C, and then the other. In row (a) of Fig. 11 the Lorenz manifold $W^s(\mathbf{0})$ is shown only up to geodesic distance 31 when it intersects Σ_ϱ in a single curve W^s_1, which is invariant under the rotation symmetry. Note that all points on $W^s_1 \subset W^s(\mathbf{0}) \cap \Sigma_\varrho$ do not return to Σ_ϱ but flow directly to $\mathbf{0}$; this is consistent with the fact that the flow points down in this region of Σ_ϱ. In row (b) $W^s(\mathbf{0})$ is computed up to geodesic distance 62. There are now two additional pairs of (symmetrically related) intersection curves with Σ_ϱ; we can speak of a second and third pair of intersection curves, W^s_2 and W^s_3.

We remark that the first-return map to Σ_ϱ maps curves in $W^s(\mathbf{0}) \cap \Sigma_\varrho$ to each other in quite an involved fashion. Notice that the first (symmetric) intersection curve W^s_1 as well as the third pair of intersection curves W^s_3 are entirely contained in the region where the flow points down. On the other hand, W^s_2 crosses C; let us denote the two (symmetrically related) intersection points of $W^s_2 \cap C$ by $w^\pm_C$. The (open) segment on W^s_2 that lies in the region where the flow points down maps under the first-return map to the (open) segment on W^s_2 that lies in the region where the flow points up, which then subsequently maps to W^s_1. More specifically, the image on W^s_1 of each of the two curves of the pair W^s_2 extends from the image of $w^\pm_C$ to infinity (in the direction $y \to \pm\infty$). The third intersection curve W^s_3 and the segment of W^s_2 that lies in the region where the flow points down should be

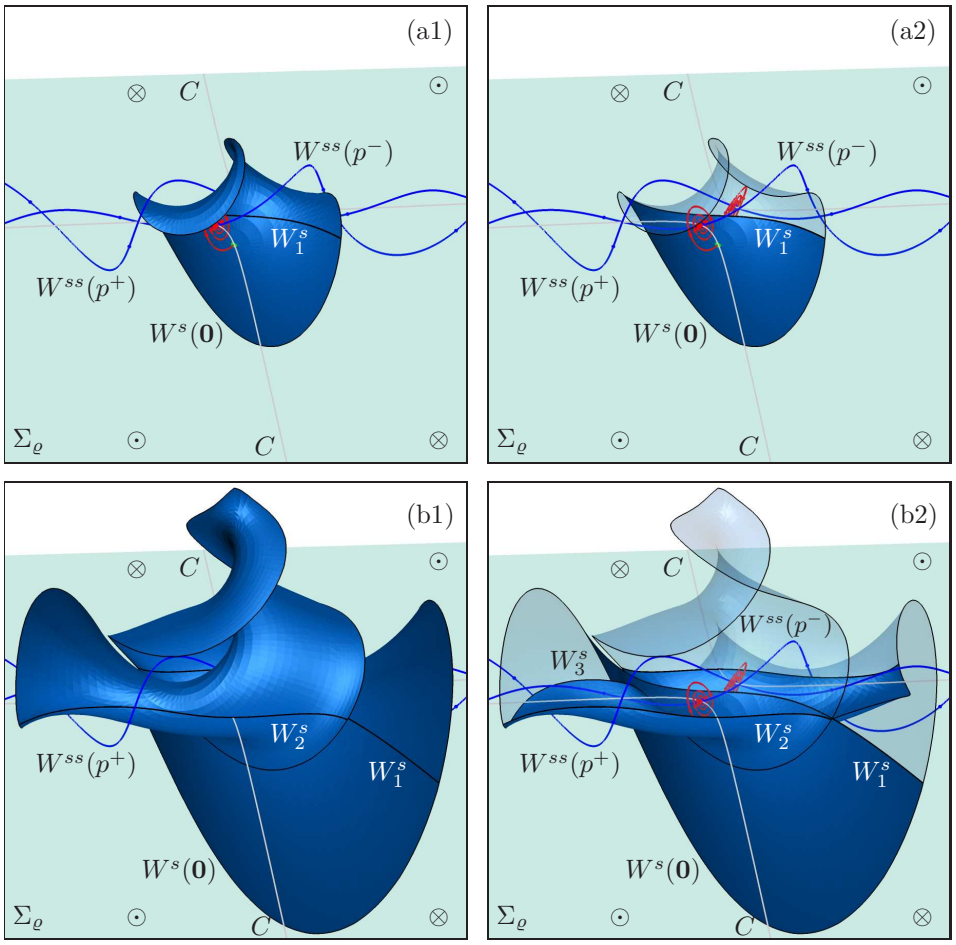

FIGURE 11. Intersection curves of $W^s(\mathbf{0})$ for $\varrho = 10$ with the section Σ_ϱ arise as the manifold grows during the compuation. Row (a) shows $W^s(\mathbf{0})$ up to geodesic distance 31, and row (b) up to geodesic distance 62. The manifold $W^s(\mathbf{0})$ is show on the left as a solid surface, while on the right the part of $W^s(\mathbf{0})$ above the section is rendered transparent; also shown are the one-dimensional objects from Fig. 9. The curves labeled C divide Σ_ϱ into regions where the flow points up ($\odot$) and down ($\otimes$), respectively.

thought of as connected. In fact, one should identify the two 'closest' limits of W^s_2 as $y \to \pm\infty$ and of W^s_3 as $y \to \mp\infty$ (as they correspond to the same sheet of $W^s(\mathbf{0})$); see Fig. 11(b). Together these two curves cover the segment of W^s_1 between the image of $w^{\pm}_C$ and its limit $y \to \mp\infty$. Finally, note that the segment on W^s_1 that is bounded by the two symmetric points $w^{\pm}_C$ contains the central point $(0, 0, 9) \in W^s_1$ on the z-axis, which does not have a pre-image in Σ_ϱ.

Figure 12 shows the intersection of $W^s(\mathbf{0})$ with Σ_ϱ for $\varrho = 10$, up to geodesic distance 150 as in Figure 10(a). There are now a lot more intersection curves, and their mapping behavior under the first-return map is equally involved and similar

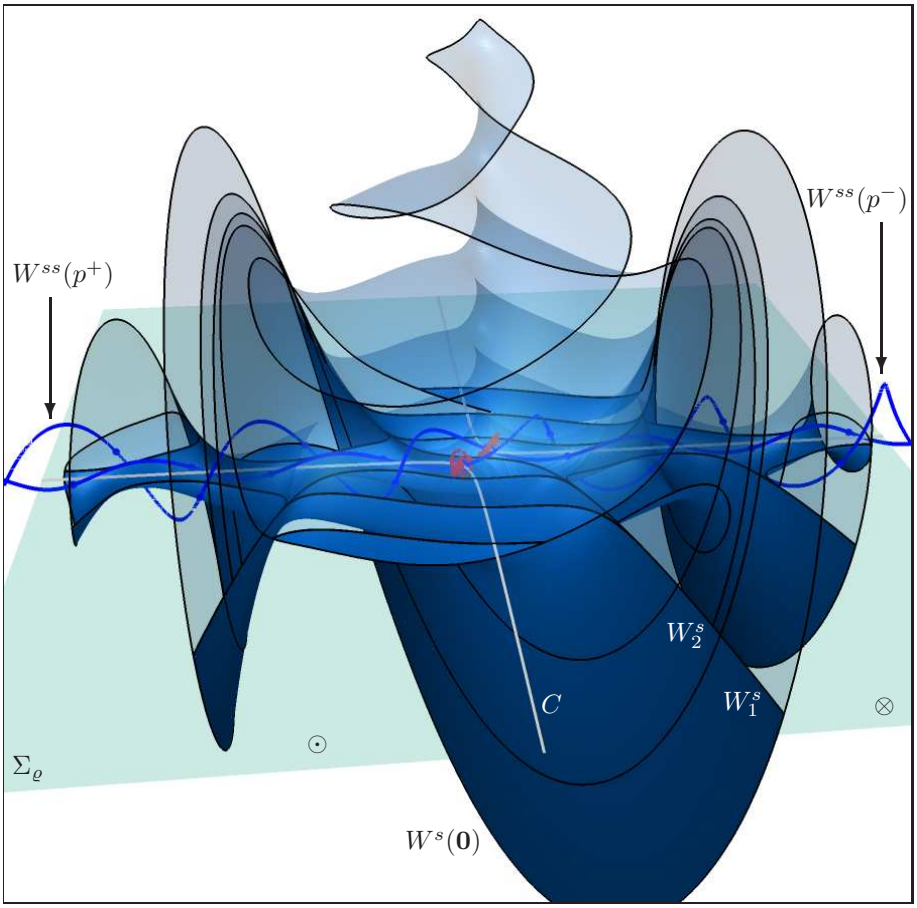

FIGURE 12. The manifolds $W^s(\mathbf{0})$ (up to geodesic distance 150), $W^{ss}(p^\pm)$ and $W^u(\mathbf{0})$, and their intersections with the section Σ_ϱ for $\varrho = 10$.

to that of the curves W^s_2 and W^s_3 from Fig. 11. Notice further that both branches of $W^{ss}(p^\pm)$ wind around C, where the branch of $W^{ss}(p^+)$ with $x \to -\infty$ and the branch of $W^{ss}(p^+)$ with $x \to +\infty$ is further out. Clearly, $W^s(\mathbf{0})$ and $W^{ss}(p^\pm)$ cannot intersect and $W^s(\mathbf{0})$ winds around the inner branches of $W^{ss}(p^\pm)$, while the outer branches of $W^{ss}(p^\pm)$ wind around $W^s(\mathbf{0})$.

The two-dimensional manifold $W^s(\mathbf{0})$ acts as a separatrix of the two basins of the attracting equilibria $p^\pm$ under the flow of (13), which are connected open regions that contain the one-dimensional manifolds $W^{ss}(p^\pm)$. However, it is not easy to distinguish the two basins in Fig. 12. Therefore, Fig. 13 shows the two corresponding intersections $\mathcal{B}(p^\pm) \subset \Sigma_\varrho$ of the basins with the section for $\varrho = 10$. Note that $\mathcal{B}(p^\pm)$ are basins of $p^\pm$ under the first return map to Σ_ϱ. These basins in Σ_ϱ consist of infinitely many connected components, and their union is dense in Σ_ϱ. The connected components are bounded by curves in $W^s(\mathbf{0}) \cap \Sigma_\varrho$; all these curves tend to infinity along two limiting directions. With the exception of the symmetric curve W^s_1, the end points of each curve in $W^s(\mathbf{0}) \cap \Sigma_\varrho$ tend to infinity either both in the direction of positive y (for curves in the region of positive y), or both in the

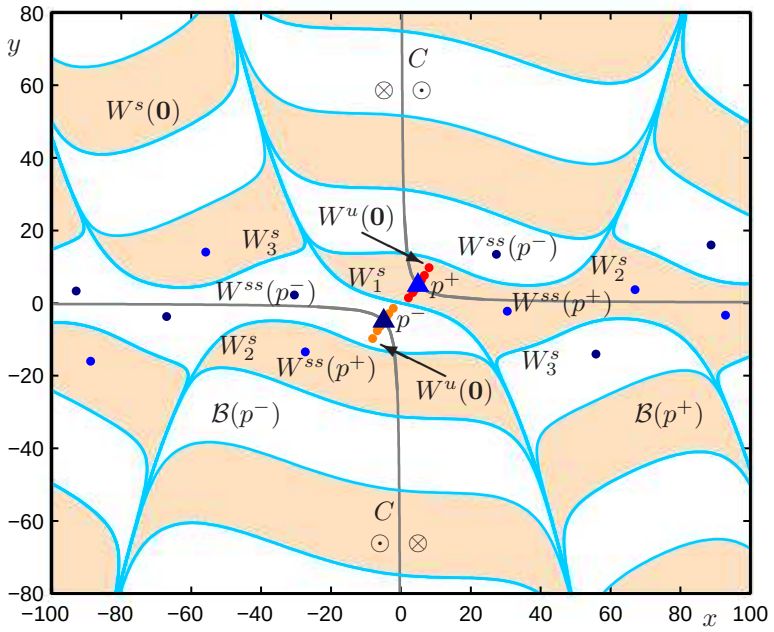

FIGURE 13. Intersections of the manifolds $W^s(\mathbf{0})$, $W^u(\mathbf{0})$ and $W^{ss}(p^\pm)$ with the section Σ_ϱ for $\varrho = 10$; the basin $\mathcal{B}(p^+)$ is shaded.

direction of negative y (for curves in the region of negative y). As a result, each component of $\mathcal{B}(p^\pm)$ extends to infinity along extremely narrow channels, formed in between two boundary curves in $W^s(\mathbf{0}) \cap \Sigma_\varrho$ that tend to infinity along the same direction. The two connected components that contain p^+ and p^-, respectively, are the immediate basins, and they also contain all intersection points of the respective inner branch of $W^{ss}(p^\pm)$. Furthermore, the intersection points of the branch of $W^u(\mathbf{0})$ that leaves the neighborhood of $\mathbf{0}$ in the direction of positive x lie entirely in the immediate basin of p^+, while the other branch of $W^u(\mathbf{0})$ lies entirely in the immediate basin of p^-.

4.4. **Intersection of $W^s(\mathbf{0})$ with Σ_ϱ for $\varrho = 20$.** We now consider corresponding images for a ϱ-value after the homoclinic bifurcation, where we choose $\varrho = 20$ as before. Figure 14 shows the intersection of $W^s(\mathbf{0})$ with Σ_ϱ for $\varrho = 20$, up to geodesic distance 148.75 as in Fig. 10(b). Also shown in Fig. 14 are the one-dimensional strong stable manifolds $W^{ss}(p^+)$, the unstable manifold $W^u(\mathbf{0})$ and the periodic orbits $\Gamma^\pm$. The positions of $W^{ss}(p^\pm)$ has not changed qualitatively: there are still inner and outer branches of these manifolds that spiral around C as before. However, the Lorenz manifold $W^s(\mathbf{0})$ does not spiral around the respective branches as before; compare Fig. 14 with Fig. 12. This change goes along with a change of the intersection curves in $W^s(\mathbf{0}) \cap \Sigma_\varrho$. Figure 14 shows that there are a lot more (in fact, infinitely many) sheets of $W^s(\mathbf{0})$ in between the respective branches of $W^{ss}(p^\pm)$.

Figure 14 shows already that the role of $W^s(\mathbf{0})$ as basin boundary of $p^\pm$ has changed. To investigate this in more detail, we show in Fig. 15(a) the curves in $W^s(\mathbf{0}) \cap \Sigma_\varrho$. One immediately notices the difference with Fig. 13. The 'outer-most

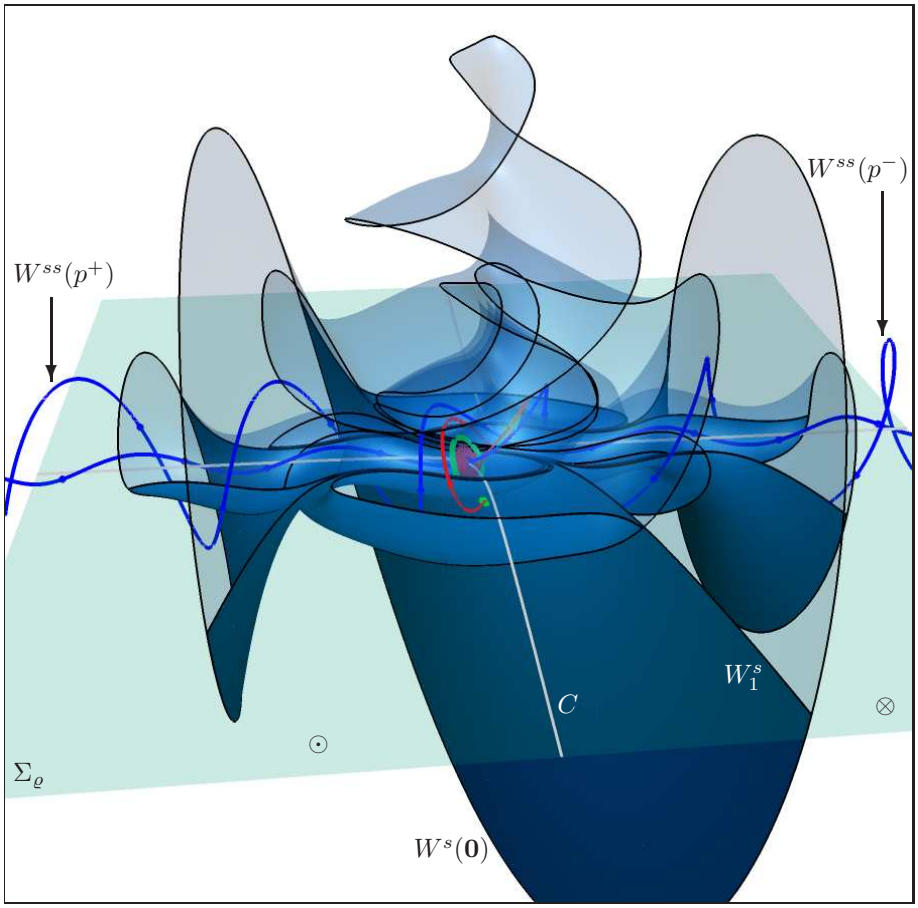

FIGURE 14. The manifolds $W^s(\mathbf{0})$ (up to geodesic distance 148.75), $W^u(\mathbf{0})$ and $W^{ss}(p^\pm)$, and their intersections with the section Σ_ϱ for $\varrho = 20$.

layer' of curves in $W^s(\mathbf{0}) \cap \Sigma_\varrho$ for $\varrho = 20$ are geometrically as for $\varrho = 10$. However, the 'inner-most layer' of curves in $W^s(\mathbf{0}) \cap \Sigma_\varrho$ has changed dramatically. These inner curves are not like W^s_2 and W^s_3 from Figs. 12 and 13, but they cross from the region of positive y to the region of negative y by passing very close to the symmetric curve W^s_1. In the process, these inner intersection curves in $W^s(\mathbf{0}) \cap \Sigma_\varrho$ accumulate on the boundary of two regions — the two immediate basins of p^+ and p^-, respectively. The two immediate basins again contain infinitely many intersection points of $W^u(\mathbf{0}) \cap \Sigma_\varrho$. However, now the first intersection point of $W^u(\mathbf{0})$ with the section Σ_ϱ does not lie in the immediate basin and all subsequent points of $W^u(\mathbf{0}) \cap \Sigma_\varrho$ lie on the other side of the central symmetric curve W^s_1. This is due to the fact that the branch of $W^u(\mathbf{0})$ that leaves the neighborhood of $\mathbf{0}$ in the direction of positive x now lies entirely in the basin of p^-, and vice versa; compare with Fig. 9(c).

4.5. **Bifurcation of the basins $\mathcal{B}(p^\pm)$.** It is a key realization from Fig. 15 that the basins $\mathcal{B}(p^\pm) \subset \Sigma_\varrho$ are no longer bounded by the two-dimensional manifold $W^s(\mathbf{0})$

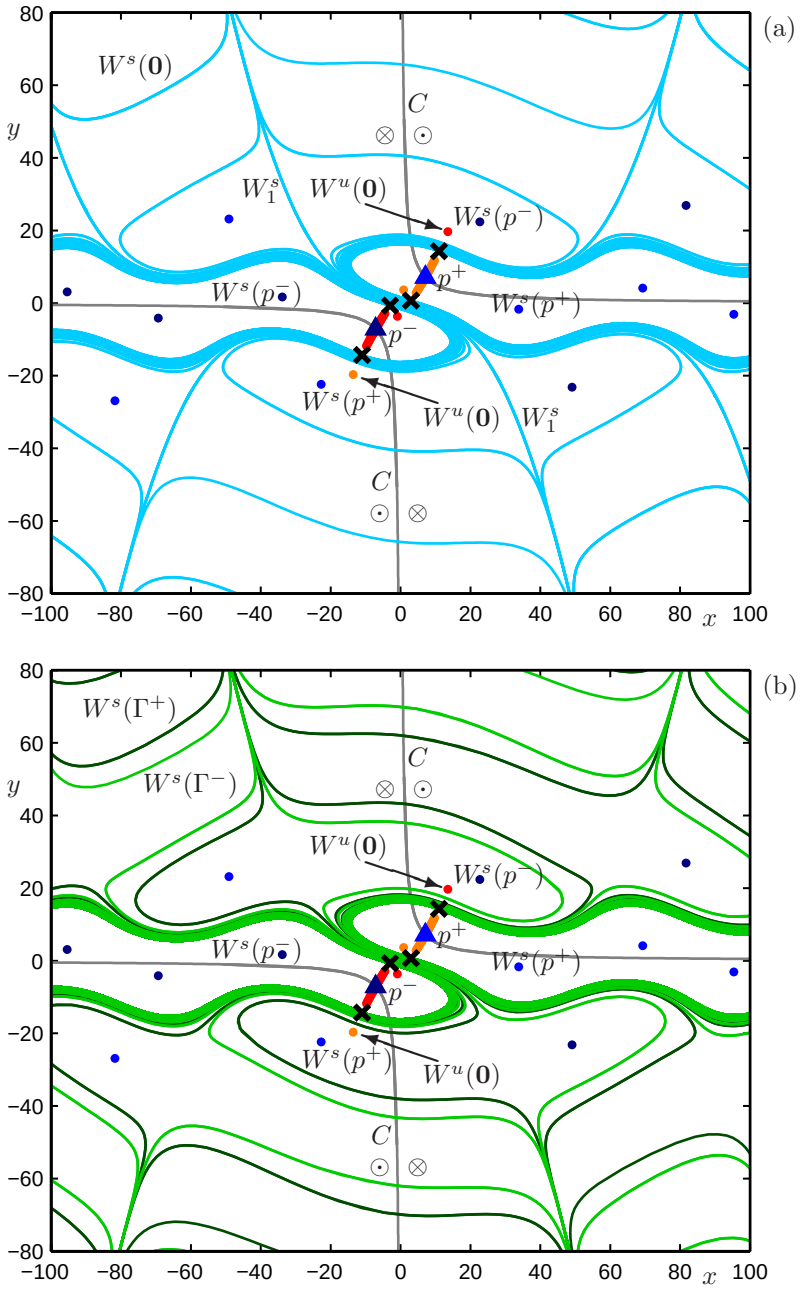

FIGURE 15. Intersections of manifolds with the section Σ_ϱ for $\varrho = 20$. Panel (a) shows $W^s(\mathbf{0})$, and panel (b) shows $W^s(\Gamma^+)$ (darker curves) and $W^s(\Gamma^-)$ (lighter curves); also shown are the intersection points of $W^{ss}(p^\pm)$, $W^u(\mathbf{0})$ and $\Gamma^\pm$ (black crosses).

alone. Rather, they are bounded (at least near $p^\pm$) by the stable manifolds $W^s(\Gamma^\pm)$ of the two saddle periodic orbits $\Gamma^\pm$. The black crosses in Fig. 15 are the two pairs

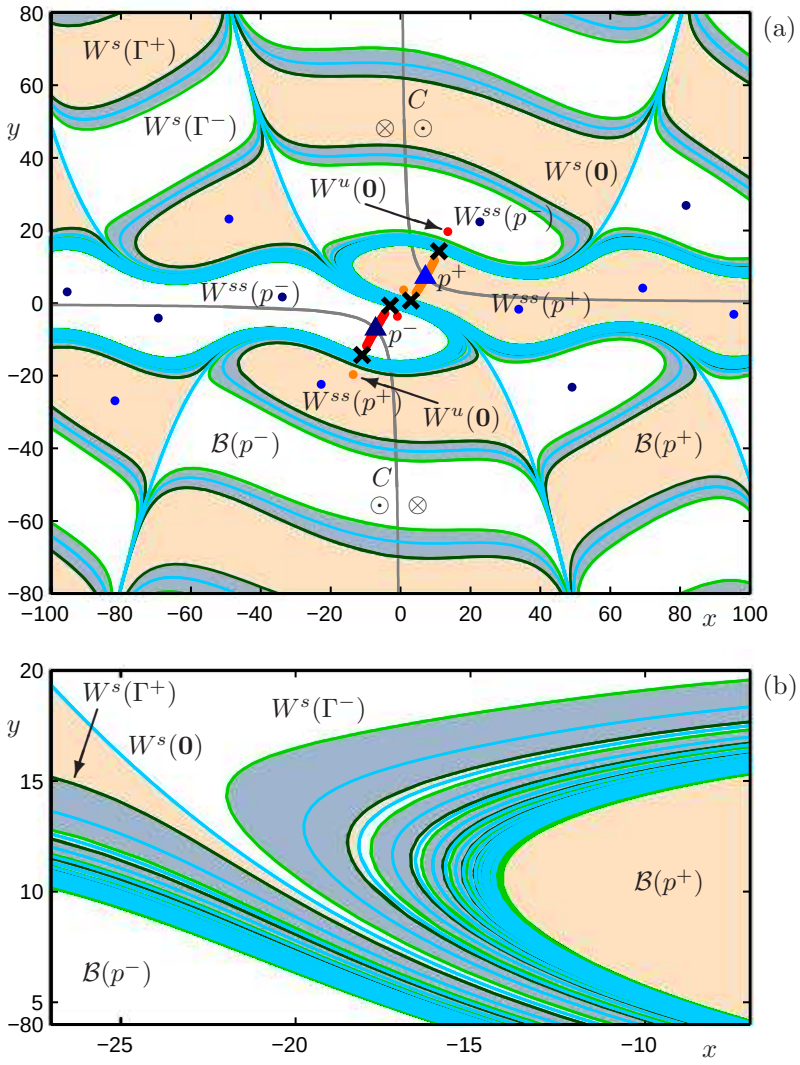

FIGURE 16. Panel (a) shows how the curves in $W^s(\mathbf{0}) \cap \Sigma_\varrho$ and in $W^s(\Gamma^\pm) \cap \Sigma_\varrho$ bound the basins $\mathcal{B}(p^+)$ (light shading) and of $\mathcal{B}(p^-)$ (white). The narrow regions (darker shading) are channels of preturbulence, where all manifolds accumulate on the boundary of $\mathcal{B}(p^\pm)$; also shown are $W^{ss}(p^\pm)$, $W^u(\mathbf{0})$ and $\Gamma^\pm$. Panel (b) is an enlargement near the symmetric curve $W^s_1 \subset W^s(\mathbf{0}) \cap \Sigma_\varrho$.

of intersection points of $\Gamma^\pm$ with Σ_ϱ, and panel (b) shows a set of intersection curves in $W^s(\Gamma^\pm) \cap \Sigma_\varrho$. Notice that these curves run 'in parallel' on either side of corresponding curves in $W^s(\Gamma^\pm) \cap \Sigma_\varrho$, shown in panel (a). Furthermore, the curves in $W^s(\Gamma^+) \cap \Sigma_\varrho$ are images of the curves in $W^s(\Gamma^-) \cap \Sigma_\varrho$ under the rotational symmetry; in particular, this means that there is no curve in Fig. 15(b) that is itself symmetric.

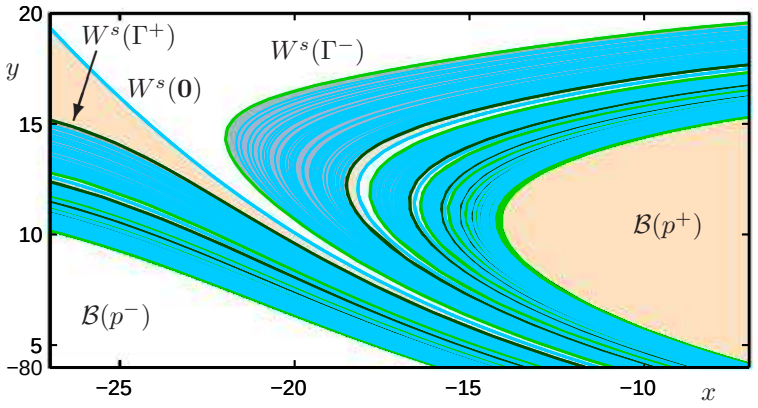

FIGURE 17. Additional curves in $W^s(\mathbf{0}) \cap \Sigma_\varrho$ inside the channels of preturbulence.

To illustrate the structure of the basins $\mathcal{B}(p^\pm) \subset \Sigma_\varrho$ for $\varrho = 20$, Fig. 16 shows the curves from Fig. 15(a) and (b) in the same plot. The situation is rather complicated. The immediate basin of p^+ is bounded by a single curve in $W^s(\Gamma^+) \cap \Sigma_\varrho$. This is not easy to see in Fig. 16(a) because curves in $W^s(\Gamma^-) \cap \Sigma_\varrho$ and in $W^s(\Gamma^+) \cap \Sigma_\varrho$ accumulate on this boundary curve, as do curves in $W^s(\mathbf{0}) \cap \Sigma_\varrho$. The entire basin $\mathcal{B}(p^+)$ consists again of infinitely many regions. We can distinguish larger (lightly shaded) regions in Fig. 16, which are somewhat smaller, but similar to those of $\mathcal{B}(p^+)$ for $\varrho = 10$ in Fig. 13. In between these larger regions in Fig. 16 we find channels (darker shading) that are bounded by a curve in $W^s(\Gamma^+) \cap \Sigma_\varrho$ and a curve in $W^s(\Gamma^-) \cap \Sigma_\varrho$, and divided by a curve in $W^s(\mathbf{0}) \cap \Sigma_\varrho$. As the enlargement in Fig. 16(b) shows, the boundary of the immediate basin of $p+$ is locally the limit of an alternating sequence of a strip in $\mathcal{B}(p^+)$, a strip in $\mathcal{B}(p^-)$, a strip of a channel, and so on. Given the symmetry of Fig. 15, the corresponding statements holds for the boundary of the immediate basin of p^-.

We refer to the channels in Fig. 16 as *channels of preturbulence* for the following reason. Consider a point ξ on the boundary of, say, $\mathcal{B}(p^+)$ that is formed by a curve of $W^s(\Gamma^+) \cap \Sigma_\varrho$. Such a point ξ is eventually mapped, after a certain number N of iterates of the first-return map to Σ_ϱ, to the boundary of the immediate basin. We assume further that ξ is typical, in the sense that it does not lie on the tangency locus C or any of its pre-images. Then the Nth-return map to Σ_ϱ maps a sufficiently small neighborhood of ξ diffeomorphically to its image in Σ_ϱ, which is a neighborhood of a point on the immediate basin of p^+. Hence, the boundary curve of $\mathcal{B}(p^+)$ on which ξ lies must also be accumulated (on one side) by curves in $W^s(\Gamma^+) \cap \Sigma_\varrho$, in $W^s(\Gamma^-) \cap \Sigma_\varrho$ and in $W^s(\mathbf{0}) \cap \Sigma_\varrho$. In other words, the channels of preturbulence in Fig. 16 need to be filled in recursively by accumulating and increasingly narrow regions in both $\mathcal{B}(p^+)$ and $\mathcal{B}(p^-)$. The recursive nature of this accumulation is apparent from Fig. 16(b): every grey channel of preturbulence needs to be 'filled in' with a diffeomorphic image of the entire image.

The set of curves in $W^s(\Gamma^\pm) \cap \Sigma_\varrho$ that we computed and show in Figs. 15(b) and 16 allow us to identify a repeated accumulation process of the two basins on their own boundary. As our figures show, in the narrow channels of preturbulence it is practically impossible to decide whether a given initial condition will end up in

$\mathcal{B}(p^+)$ or in $\mathcal{B}(p^-)$. This phenomenon co-exists with the larger regions of $\mathcal{B}(p^+)$ or in $\mathcal{B}(p^-)$, where the dynamics is highly predictable. The local structure of the channels of preturbulence is that of a Cantor set of curves that bound $\mathcal{B}(p^+)$ and $\mathcal{B}(p^-)$. Hence, there are infinitely many more curves of $W^s(\mathbf{0}) \cap \Sigma_\varrho$ and $W^s(\Gamma^\pm) \cap \Sigma_\varrho$ in each channel, which can also be computed with our method. As an example, Fig. 17 shows how curves of $W^s(\mathbf{0}) \cap \Sigma_\varrho$ accumulate on each other inside the channels of preturbulence to form a Cantor set of curves; compare with Fig. 16.

The manifold computations allow us to state clearly how preturbulence arises in the Lorenz system and how it manifests itself after the homoclinic explosion point. Our findings can be summarized as follows.

Result. (transition to preturbulence)

Consider the Lorenz system (13) with $\sigma = 10$ and $\beta = 8/3$. For $1 < \varrho < \varrho_{\text{het}} \approx 24.0579$ the equilibria $p^\pm$ are the only attractors of the Lorenz system, and the union of their two basins is dense in $\mathbb{R}^3$.

(L1) For $1 < \varrho < \varrho_{\text{hom}} \approx 13.9162$ the boundary between the basins of p^+ and p^- is formed by $W^s(\mathbf{0})$.

(L2) For $\varrho_{\text{hom}} < \varrho < \varrho_{\text{het}} \approx 24.0579$ the two basins of p^+ and p^- are bounded by $W^s(\mathbf{0})$ and $W^s(\Gamma^+)$, and by $W^s(\mathbf{0})$ and $W^s(\Gamma^-)$, respectively. Furthermore, the basin of p^+ accumulates on one side onto the boundary $W^s(\Gamma^-)$ of the basin of p^-, and vice versa. The result is a local Cantor structure of basin boundaries, organised in narrow channels of preturbulence, where trajectories can be found that have arbitrarily long transients before ending up at either p^+ or p^-.

(L3) As ϱ_{hom} is approached from above the manifolds $W^s(\Gamma^\pm)$ and, hence, the channels of preturbulence, converge to $W^s(\mathbf{0})$.

For completeness, we state (without presenting computed images) what happens to the two-dimensional invariant manifolds as ϱ is increased further into the region of full-blown chaotic dynamics, as can be found for $\varrho = 28$.

Result. (transition to chaos)

Consider the Lorenz system (13) with $\sigma = 10$ and $\beta = 8/3$.

(L3) At $\varrho = \varrho_{\text{het}}$ there is a symmetric pair of heteroclinic cycles between $\Gamma^\pm$ and the origin $\mathbf{0}$ [15]. As ϱ_{het} is approached, the channels of preturbulence become larger and the Cantor structure of basin boundaries inside them becomes 'fatter' (in Hausdorff dimension [51]), until it has full measure for $\varrho = \varrho_{\text{het}}$.

(L4) For $\varrho_{\text{het}} < \varrho < \varrho_{\text{H}} = \frac{470}{19} \approx 24.736842$ there are three attractors: the equilibria $p^\pm$ and a chaotic attractor. The basin of the chaotic attractor is the continuation of the channels of preturbulence. The boundary between the basins is formed by $W^s(\Gamma^\pm)$, and the Lorenz manifold $W^s(\mathbf{0})$ is dense in the basin of the chaotic attractor.

(L5) The manifolds $W^s(\Gamma^\pm)$ and, hence, the basins of $p^\pm$ shrink to $W^{ss}(p^\pm)$ as the Hopf bifurcation at ϱ_{H} is approached. For ϱ past ϱ_{H} the chaotic attractor is the only attractor and $W^s(\mathbf{0})$ is dense in $\mathbb{R}^3$.

These results on the transition to turbulence via preturbulence in the Lorenz system agree with the numerical study in [69] of decay times to the two attracting equilibria for $\varrho > \varrho_{\text{hom}}$; they were found to increase with ϱ and then tend to infinity as ϱ_{het} is approached. In fact, our results explain the sensitivity on the initial

condition in the preturbulent regime as the result of the accumulation of the two basins of p^+ and p^- onto each other's boundary.

The fact that $W^s(\mathbf{0})$ is dense in the phase space $\mathbb{R}^3$ for $\varrho > \varrho_{\rm H}$ is a direct consequence of sensitive dependence on the initial condition in the chaotic regime of the Lorenz system. Given any point $r \notin W^s(\mathbf{0})$, consider an ε-neighborhood $N_\varepsilon(r)$ of r. Then $W^s(\mathbf{0})$ must intersect $N_\varepsilon(r)$, because otherwise all points in $N_\varepsilon(r)$ would have the same itineary (in violation of sensitive dependence on the initial condition) as they approach and then follow the chaotic attractor. Since $\varepsilon > 0$ is arbitrary, the denseness of $W^s(\mathbf{0})$ in $\mathbb{R}^3$ follows. Depending on one's point of view, this property of $W^s(\mathbf{0})$ can be seen equivalently as the reason for — or the logical consequence of — sensitive dependence on the initial condition.

5. **Conclusions.** We demonstrated that the computation of two-dimensional manifolds and their intersection curves with a suitable cross-section is a powerful tool for understanding the changes of the dynamics that are brought about by global bifurcations. In particular, this appraoch allows one to determine how basins of different attractors change topologically. Such computations can be performed in an efficient and accurate way via the continuation of solution families of suitably defined boundary value problems. We demonstrated this here with two examples. Firstly, we showed how the stable manifold changes in a Shilnikov bifurcation to form a basin of a bifurcating stable periodic orbit. Secondly, we considered the homoclinic explosion in the Lorenz system and showed how preturbulence arises via a dramatic change of the basins of the two stable attracting equilibria.

The technique presented here offers the possibility to investigate the geometry of two-dimensional invariant manifolds near any global bifurcation of three-dimensional vector fields. Following on from the study of the simple Shilnikov bifurcation, we are presently considering homoclinic bifurcations of a saddle equilibrium of a generic vector field in $\mathbb{R}^3$. First of all, there is the chaotic case of the Shilnikov bifurcation, as well as n-homoclinic orbits to a saddle focus (where the connection back to the equilibrium occurs only after $n-1$ close passes near it). These global bifurcations can all be found in the laser system (10), where they are closely related to the phenomenon of multi-pulse excitability [67]. Furthermore, we are studying the geometry of two-dimensional stable manifolds near a homoclinic bifurcation of an equilibrium with three real eigenvalues. There are a number of different cases; in particular, the stable manifold of the saddle point may be orientable or nonorientable at the homoclinic bifurcation. Of special interest in this context are codimension-two orbit flip and inclination flip bifurcations, which give rise to a transition between these two topologically different cases [29, 30]. More generally, it will also be interesting to consider heteroclinic connections that involve any number of equilibria and/or periodic orbits. Examples of such global bifurcations can be found, for example, in [30, 39, 59].

The Lorenz system is also the subject of an ongoing project. We already mentioned briefly that the transition to attracting chaotic dynamics occurs at the heteroclinic connection between the origin and the symmetric pair of periodic orbits $\Gamma^\pm$. How the respective two-dimensional manifold change geometrically in this transition will be presented elsewhere. What is more, several other global bifurcations are encountered when the Rayleigh number is increased further [15, 60, 56]. In particular, there are (infinitely many) homoclinic orbits that close up only after a

fixed number of rotations around the secondary equilibria, as described by well-defined symbol sequences. The computational methods presented here will allow us to study in detail the consequences of these global bifurcations for the dynamics of the Lorenz system throughout its three-dimensional phase space.

Finally, we mention that it is often of interest to determine the exact shape of stable and/or an unstable manifolds arising in concrete applications. For example, the stable manifold of a saddle point or saddle periodic orbit may form the threshold for excitability [38], the boundary that determines successful transition from hyperpolarized to depolarized phases in neuron cells [61], or the limit of stable operation in power system models [6]. Another concrete application in the context of Hamiltonian systems is space mission design. The basic idea here is that stable and unstable manifolds of special solutions, for example, of libration points and nearby halo orbits, can be used for the purpose of space craft transfer with minimal energy [24]. Recent detailed studies of saddle periodic orbits in the restricted three-body problem [16, 17] would form a natural starting point for the investigation of associated stable and unstable manifolds. The BVP methods we presented allow one to determine manifolds of interest in model vector fields arising in such concrete application contexts. An advantage here is that the continuation of orbit segments generally deals effectively with sensitivity issues that arise, for example, due to the presence of different time scales.

Acknowledgments. The research of P.A. was supported by a CONICYT and an ORS grant, that of E.J.D. by an NSERC (Canada) Discovery Grant, and that of H.M.O. by an EPSRC Advanced Research Fellowship grant. Furthermore, B.K and H.M.O. acknowledge hospitality and support from Concordia University, where part of this work was carried out.

REFERENCES

[1] R. H. Abraham and C. D. Shaw, "Dynamics — The Geometry Of Behavior, Part Three: Global Behavior," Aerial Press, Santa Cruz, 1985.

[2] U. M. Ascher, J. Christiansen and R. D. Russell, *Colsys — A collocation code for boundary-value problems*, Lecture Notes in Computer Science, **76** (1979), 164–185.

[3] U. M. Ascher and R. J. Spiteri, *Collocation software for boundary value differential-algebraic equations*, SIAM J. Sci. Comput., **15** (1994), 938–952.

[4] M. R. Bassett and J. L. Hudson, *Shil'nikov chaos during copper electrodissolution*, J. Phys. Chem., **92** (1988), 6963–6966.

[5] W.-J. Beyn, *On well-posed problems for connecting orbits in dynamical systems*, in "Chaotic Numerics (Geelong, 1993)," Contemp. Math., **172**, Amer. Math. Soc., (1994), 131–168.

[6] C. J. Budd and J. P. Wilson, *Bogdanov-Takens bifurcation points and Shilnikov homoclinicity in a simple power system model of voltage collapse*, IEEE Trans. Circuits Systems I, **43** (2002), 575–590.

[7] A. R. Champneys, V. Kirk, E. Knobloch, B. E. Oldeman and J. Sneyd, *When Shil'nikov meets Hopf in excitable systems*, SIAM J. Appl. Dyn. Syst., **6** (2007), 663–693.

[8] A. R. Champneys, Y. Kuznetsov and B. Sandstede, *A numerical toolbox for homoclinic bifurcation analysis*, Int. J. Bifurc. Chaos, **6** (1996), 867–887.

[9] B. Deng and G. Hines, *Food chain chaos due to Shilnikov's orbit*, Chaos, **12** (2002), 533–538.

[10] A. Dhooge, W. Govaerts and Yu. A. Kuznetsov, *MATCONT: A Matlab package for numerical bifurcation analysis of ODEs*, ACM Trans. Math. Software, **29** (2003), 141–164.

[11] E. J. Doedel, *AUTO: A program for the automatic bifurcation analysis of autonomous systems*, Congr. Numer., **30** (1981), 265–284.

[12] E. J. Doedel with major contributions from A. R. Champneys, T. F. Fairgrieve, Yu. A. Kuznetsov, B. Sandstede and X. J. Wang, AUTO2000 and AUTO-07P: Continuation and bifurcation software for ordinary differential equations, Department of Computer Science,

Concordia University, Montreal, Canada, 2000. Available from http://cmvl.cs.concordia.ca/auto/

[13] E. J. Doedel, *Lecture notes on numerical analysis of nonlinear equations*, in "Numerical Continuation Methods for Dynamical Systems," (eds. B. Krauskopf, H. M. Osinga and J. Galán-Vioque), Underst. Complex Syst., Springer-Verlag, New York, (2007), 1–49.

[14] E. J. Doedel and M. J. Friedman, *Numerical computation of heteroclinic orbits*, J. Comput. Appl. Math., **26** (1989), 155–170.

[15] E. J. Doedel, B. Krauskopf and H. M. Osinga, *Global bifurcations of the Lorenz manifold*, Nonlinearity, **19** (2006), 2947–2972.

[16] E. J. Doedel, R. C. Paffenroth, H. B. Keller, D. Dichmann, J. Galán-Vioque and A. Vanderbauwhede, *Computation of periodic solutions of conservative systems with application to the 3-body problem*, Internat. J. Bifur. Chaos Appl. Sci. Engrg., **13** (2003), 1353–1381.

[17] E. J. Doedel, V. Romanov, R. C. Paffenroth, H. B. Keller, D. Dichmann, J. Galán-Vioque and A. Vanderbauwhede, *Elemental periodic orbits associated with the libration points in the circular restricted 3-body problem*, Internat. J. Bifur. Chaos Appl. Sci. Engrg., **17** (2007), 2625–2677.

[18] J. P. England, B. Krauskopf and H. M. Osinga, *Computing one-dimensional global manifolds of Poincaré maps by continuation*, SIAM J. Appl. Dyn. Sys., **4** (2005), 1008–1041.

[19] J. P. England, B. Krauskopf and H. M. Osinga, *Computing two-dimensional global invariant manifolds in slow-fast systems*, Internat. J. Bifur. Chaos Appl. Sci. Engrg., **17** (2007), 805–822.

[20] J. A. Feroe, *Homoclinic orbits in a parametrized saddle-focus system*, Physica D, **62** (1993), 254–262.

[21] M. Friedman and E. J. Doedel, *Numerical computation and continuation of invariant manifolds connecting fixed points*, SIAM J. Numer. Anal., **28** (1991), 789–808.

[22] P. Glendinning and C. Sparrow, *Local and global behavior near homoclinic orbits*, J. Statist. Phys., **35** (1984), 645–696.

[23] D. Goulding, S. P. Hegarty, O. Rasskazov, S. Melnik, M. Hartnett, G. Greene, J. G. McInerney, D. Rachinskii and G. Huyet, *Excitability in a quantum dot semiconductor laser with optical injection*, Phys. Rev. Lett., **98** (2007), 153903.

[24] G. Gómez, W. S. Koon, M. W. Lo, J. E. Marsden, J. Masdemont and S. D. Ross, "Invariant Manifolds, the Spatial Three-Body Problem and Space Mission Design," Astrodynamics Specialist Meeting, Quebec City, Canada, August 2001, AAS 01-31.

[25] J. Guckenheimer and P. Holmes, "Nonlinear Oscillations, Dynamical Systems and Bifurcations of Vector Fields," 2^{nd} edition, Springer-Verlag, New York/Berlin, 1986.

[26] M. E. Henderson, *Multiple parameter continuation: Computing implicitly defined k-manifolds*, Internat. J. Bifur. Chaos Appl. Sci. Engrg., **12** (2002), 451–476.

[27] M. E. Henderson, *Computing invariant manifolds by integrating fat trajectories*, SIAM J. Appl. Dyn. Sys., **4** (2005), 832–882.

[28] M. W. Hirsch, C. C. Pugh and M. Shub, "Invariant Manifolds," Lecture Notes in Mathematics, Vol. **583**, Springer-Verlag, Berlin, 1977.

[29] A. J. Homburg and B. Krauskopf, *Resonant homoclinic flip bifurcations*, J. Dynam. Diff. Eqs, **12** (2000), 807–850.

[30] A. J. Homburg and B. Sandstede, *Homoclinic and heteroclinic bifurcations in vector fields*, in B. Fiedler (Ed.) "Handbook of Dynamical Systems III" North Holland, Amsterdam (to appear); available from http://www.dam.brown.edu/people/sandsted/publications.php.

[31] J. L. Kaplan and J. A. Yorke, *Preturbulence: A regime observed in a fluid flow model of Lorenz*, Commun. Math. Phys., **67** (1979), 93–108.

[32] B. Krauskopf and H. M. Osinga, *Growing 1D and quasi-2D unstable manifolds of maps*, J. Comput. Phys., **146** (1998), 406–419.

[33] B. Krauskopf and H. M. Osinga, *Two-dimensional global manifolds of vector fields*, Chaos, **9** (1999), 768–774.

[34] B. Krauskopf and H. M. Osinga, *Computing geodesic level sets on global (un)stable manifolds of vector fields*, SIAM J. Appl. Dyn. Sys., **2** (2003), 546–569.

[35] B. Krauskopf and H. M. Osinga, *Computing invariant manifolds via the continuation of orbit segments*, in "Numerical Continuation Methods for Dynamical Systems," (eds. B. Krauskopf, H. M. Osinga and J. Galán-Vioque), Underst. Complex Syst., Springer-Verlag, New York, (2007), 117–154.

[36] B. Krauskopf, H. M. Osinga and E. J. Doedel, *Visualizing global manifolds during the transition to chaos in the Lorenz system*, in "Topology-Based Methods in Visualization II" (eds. H.-C. Hege, K. Polthier and G. Scheuermann), Mathematics and Visualization, Springer-Verlag, Berlin, (2009), 115–126.

[37] B. Krauskopf, H. M. Osinga, E. J. Doedel, M. E. Henderson, J. Guckenheimer, A. Vladimirsky, M. Dellnitz and O. Junge, *A survey of methods for computing (un)stable manifolds of vector fields*, Internat. J. Bifur. Chaos Appl. Sci. Engrg., **15** (2005), 763–791.

[38] B. Krauskopf, K. Schneider, J. Sieber, S. M. Wieczorek and M. Wolfrum, *Excitability and self-pulsations near homoclinic bifurcations in semiconductor lasers*, Optics Communications, **215** (2003), 230–249.

[39] B. Krauskopf and T. Riess, *A Lin's method approach to finding and continuing heteroclinic orbits connections involving periodic orbits*, Nonlinearity, **21** (2008), 1655–1690.

[40] Yu. A. Kuznetsov, "CONTENT – Integrated Environment for Analysis of Dynamical Systems. Tutorial," École Normale Supérieure de Lyon, Rapport de Recherche UPMA-98-224, 1998.

[41] Yu. A. Kuznetsov, "Elements of Applied Bifurcation Theory," 3^{rd} edition, Springer-Verlag, New York/Berlin, 2004.

[42] C. M. Lee, P. J. Collins, B. Krauskopf and H. M. Osinga, *Tangency bifurcations of global Poincaré maps*, SIAM J. Appl. Dyn. Syst., **7** (2008), 712–754.

[43] X.-B. Lin, *Using Melnikov's method to solve Shilnikov's problems*, Proc. R. Soc. Edinb. A, **116** (1990), 295–325.

[44] E. N. Lorenz, *Deterministic nonperiodic flows*, J. Atmosph. Sci., **20** (1963), 130–141.

[45] T. Noh, *Shilnikov's chaos in the oxidation of formic acid with bismuth ion on Pt ring electrode*, Electrochimica Acta, **54** (2009), 3657–3661.

[46] B. E. Oldeman, A. R. Champneys and B. Krauskopf, *Homoclinic branch switching: A numerical implementation of Lin's method*, Internat. J. Bifur. Chaos Appl. Sci. Engrg., **13** (2003), 2977–2999.

[47] H. M. Osinga and B. Krauskopf, *Visualizing the structure of chaos in the Lorenz system*, Computers and Graphics, **25** (2002), 815–823.

[48] H. M. Osinga and B. Krauskopf, *Crocheting the Lorenz manifold*, The Mathematical Intelligencer, **26** (2004), 25–37.

[49] H. M. Osinga and B. Krauskopf, *Visualizing curvature on the Lorenz manifold*, Journal of Mathematics and the Arts, **1** (2007), 113–123.

[50] J. Palis and W. de Melo, "Geometric Theory of Dynamical Systems," Springer-Verlag, New York/Berlin, 1982.

[51] J. Palis and F. Takens, "Hyperbolicity & Sensitive Chaotic Dynamics at Homoclinic Bifurcations," Cambridge University Press, Cambridge, 1993.

[52] T. Peacock and T. Mullin, *Homoclinic bifurcations in a liquid crystal flow*, J. Fluid Mech., **432** (2001), 369-386.

[53] C. Perelló, *Intertwining invariant manifolds and Lorenz attractor*, in "Global Theory of Dynamical Systems (Proc. Internat. Conf., Northwestern Univ., Evanston, Ill., 1979)," Lecture Notes in Math., **819**, Springer-Verlag, Berlin, (1979), 375–378.

[54] M. Phillips, S. Levy and T. Munzner, *Geomview: An interactive geometry viewer*, Not. Am. Math. Soc., **40** (1993), 985–988. Available from http://www.geom.uiuc.edu/.

[55] A. M. Rucklidge, *Chaos in a low-order model of magnetoconvection*, Physica D, **62** (1993), 323–337.

[56] A. L. Shilnikov, *On bifurcations of the Lorenz attractor in the Shimizu-Morioka model*, Physica D, **62** (1993), 338–346.

[57] L. P. Shilnikov, *A case of the existence of a countable number of periodic orbits*, Sov. Math. Dokl., **6** (1965), 163–166.

[58] L. P. Shilnikov, *A contribution to the problem of the structure of an extended neighborhood of a rough state to a saddle-focus type*, Math. USSR-Sb, **10** (1970), 91–102.

[59] L. P. Shilnikov, A. L. Shilnikov, D. V. Turaev and L. Chua, "Methods of Qualitative Theory in Nonlinear Dynamics, Part II," World Scientific Series on Nonlinear Science, Series A, Vol. **5**, 2001.

[60] C. Sparrow, "The Lorenz Equations: Bifurcations, Chaos and Strange Attractors," Appl. Math. Sci. No. 41, Springer-Verlag, New York, 1982.

[61] J. V. Stern, H. M. Osinga, A. LeBeau and A. Sherman, *Resetting behavior in a model of bursting in secretory pituitary cells: Distinguishing plateaus from pseudo-plateaus*, Bulletin Math. Biology, **70** (2008), 68–88.

[62] S. H. Strogatz, "Nonlinear Dynamics and Chaos: With Applications to Physics, Biology, Chemistry and Engineering," Adison-Wesley, Reading, MA, 1994.
[63] O. Vaudel, N. Péraud and P. Besnard, *Synchronization on excitable pulses in optically injected semiconductor lasers*, Proc. SPIE, **6997** (2008), 69970F.
[64] K. Watada, T. Endo and H. Seishi, *Shilnikov orbits in an autonomous third-order chaotic phase-locked loop*, IEEE Trans. on Circ. and Syst. I, **45** (1998), 979–983.
[65] S. M. Wieczorek and B. Krauskopf, *Bifurcations of n−homoclinic orbits in optically injected lasers*, Nonlinearity, **18** (2005), 1095–1120.
[66] S. M. Wieczorek, B. Krauskopf and D. Lenstra, *A unifying view of bifurcations in a semiconductor laser subject to optical injection*, Optics Communications, **172** (1999), 279–295.
[67] S. M. Wieczorek, B. Krauskopf and D. Lenstra, *Multipulse excitability in a semiconductor laser with optical injection*, Physical Review Letters, **88** (2002), 1–4.
[68] S. M. Wieczorek, B. Krauskopf, T. B. Simpson and D. Lenstra, *The dynamical complexity of optically injected semiconductor lasers*, Phys. Reports, **416** (2005), 1–128.
[69] J. A. Yorke and E. D. Yorke, *Metastable chaos: The transition to sustained chaotic behavior in the Lorenz model*, J. Stat. Phys., **21** (1979), 263–277.

Received December 2009; revised July 2010.

E-mail address: Pablo.Aguirre@bristol.ac.uk
E-mail address: doedel@encs.concordia.ca
E-mail address: B.Krauskopf@bristol.ac.uk
E-mail address: H.M.Osinga@bristol.ac.uk